MODELING SELECTED X-RAY OBSERVATIONS OF NONMAGNETIC CATACLYSMIC VARIABLES USING XMM-NEWTON AND SWIFT OBSERVATORIES

A THESIS SUBMITTED TO
THE GRADUATE SCHOOL OF NATURAL AND APPLIED SCIENCES
OF
MIDDLE EAST TECHNICAL UNIVERSITY

BY

ARMIN NABIZADEH

IN PARTIAL FULFILLMENT OF THE REQUIREMENTS
FOR
THE DEGREE OF MASTER OF SCIENCE
IN
PHYSICS

AUGUST 2017

Approval of the thesis:

MODELING SELECTED X-RAY OBSERVATIONS OF NONMAGNETIC CATACLYSMIC VARIABLES USING XMM-NEWTON AND SWIFT OBSERVATORIES

submitted by **ARMIN NABIZADEH** in partial fulfillment of the requirements for the degree of **Master of Science in Physics Department, Middle East Technical University** by,

Prof. Dr. Gülbin Dural Ünver
Dean, Graduate School of **Natural and Applied Sciences**

Prof. Dr. Altuğ Özpineci
Head of Department, **Physics**

Prof. Dr. Şölen Balman
Supervisor, **Physics. Department, METU**

Examining Committee Members:

Prof. Dr. Nilgün Kızıloğlu
Physics Department, METU

Prof. Dr. Şölen Balman
Physics Department, METU

Prof. Dr. Sacit Özdemır
Astronomy and Space Science Dept., Ankara Univ.

Assoc. Prof. Dr. Sinan Kaan Yerli
Physics Department, METU

Assoc. Prof. Dr. Serhat Çakır
Physics Department, METU

Date: ***August 2, 2017***

I hereby declare that all information in this document has been obtained and presented in accordance with academic rules and ethical conduct. I also declare that, as required by these rules and conduct, I have fully cited and referenced all material and results that are not original to this work.

Name, Last Name: ARMIN NABIZADEH

Signature :

ABSTRACT

MODELING SELECTED X-RAY OBSERVATIONS OF NONMAGNETIC CATACLYSMIC VARIABLES USING XMM-NEWTON AND SWIFT OBSERVATORIES

Nabizadeh, Armin
M.S., Department of Physics
Supervisor : Prof. Dr. Şölen Balman

August 2017, 72 pages

Despite of recent developments in observational techniques, the diversity of the X-ray observations of nonmagnetic Cataclysmic Variables (CVs) are still not entirely understood. In this work, we plan to review the X-ray spectral characteristics of such systems during their quiescence state which in general explained by the multi-temperature plasma emission models and also, the CV spectra that show dominantly hard X-ray emission with few sources that reveal soft X-ray/EUV blackbody emission. For this purpose, we have selected several unpublished nonmagnetic CV data of three sources SS Aur, EY Cyg and TW Pic taken and archived by XMM-Newton and SWIFT Observatories. Using various data analysis techniques, we will accomplish spectral and temporal analysis for a better understanding of dwarf nova phenomenon and the nature of accretion flow and geometry in these systems.

Keywords: Cataclysmic Variables, Dwarf Novae, X-rays, Spectral Analysis, SS Aur, EY Cyg, TW Pic

ÖZ

AMANYETİK KATAKLİSMİK DEĞİŞKENLERİN X-IŞINI GÖZLEMLERİNİN XMM-NEWTON VE SWIFT UYDU VERİLERİYLE MODELLENMESİ

Nabizadeh, Armin
Yüksek Lisans, Fizik Bölümü
Tez Yöneticisi : Prof. Dr. Şölen Balman

Ağustos 2017 , 72 sayfa

Gözlemsel tekniklerdeki gelişmelere rağmen amanyetik kataklismik değişkenlerde X-ışınlarının gözlemsel çeşitliliğinin sebepleri halen anlaşılmamaktadır. Yapacağımız tez çalışmasında bu tür sistemlerin X-ışını spektral özelliklerini ele alarak durgun, yüksek fazlarında ve disk patlamalarında karşılartırmalar ile karakterizasyon yapacağız. Bununla beraber, çok-sıcaklıklı plasma emisyon modellerini ve yüksek fazlarda ve patlama evrelerinde beklenen kara cisim ışıma bileşkelerini çalışacağız. Bu doğrultuda bir takım yayınlanmış amanyetik kataklismik değişken verilerini XMM-Newton ve SWIFT arişlerinden tesbit ettik. Spektral ve temporal analiz teknikleri kullanarak cüce novaların, yüksek faz sistemlerinin ve bu tür sistemlerdeki madde aktarım akışlarının ve geometrisinin anlayışını geliştirmeyi planlamaktayız.

Anahtar Kelimeler: Kataklismik Değişkenlerde, Cüce nova, X-ışınları, tayf analizi, SS Aur, EY Cyg, TW Pic

To my beloved parents and wife...

ACKNOWLEDGMENTS

First of all, I would like to express my gratitude to Prof. Dr. Şölen Balman, my supervisor for her constant support, guidance and encouragement over the two and a half years. I had an enormous benefit from the numerous discussions we had, and I thank her for her patience. Her contribution was essential to the accomplishment of this work. Her mentorship was paramount in providing a well rounded experience consistent my long-term career goals.

I also had the chance to benefit from the great experience of my bachelor advisor, Prof. Ali Ajabshirizadeh whom I would like to thank very much for the incredible insight he offered me. I also thank Dr. Ebadi and Dr. Hosseinpour for their endless supports. I have made significant academic progress with their invaluable guidance, remarks, and recommendations.

My deepest gratitude goes to my whole family, particularly my dear parents Mehdi and Azam, for their endless love and unconditional support throughout my life. Without them, I would not be the person I am today. My special thanks are due to my elder sisters, Solmaz and Sanaz, who have a great impact on my personal development, and their husbands, Behzad and Mehdi who always strengthened my morale by standing by me in all situations.

I am also grateful to my spouse's parents Esfandiar and Shahin who are like real parents to me and also her siblings Bijan and Narmin. Their unfailing supports during these years kept me in the right direction when I was struggling to decide about my future.

I would like to express my appreciation to all my friends who have contributed directly or indirectly to this thesis. I am grateful to Shirin Sepehri, Vesal Rasoulzadeh, Nima Bonyadi, Mohammad Taher Ghalandari, Hossein Siahpoosh, Arash Nikniazi, Vahid Eghbal Akhlaghi, Majid Biazaran, Mohammad Reza Zharfa, Nastaran Deljavan, Amir Hamed Zakeri, Atefe Lafzi, Sina Milani, Fate-

meh Soleimani, Sohrab and Sahar Heidari and Parinaz Ashrafi. I always feel lucky and happy to have such supportive friends.

I am also grateful to a research scholarship through the TÜBITAK (Scientific and Technological Council of Turkey) 1001 grant project No. 114F351.

Finally, and most importantly, I would like to thank my lovely and beautiful wife Nasrin. Her support, encouragement, quiet patience and unwavering belief in me were undeniably the bedrock upon which the past eight years of my life have been built. Thank you for being my best friend. I love you always and forever.

TABLE OF CONTENTS

CHAPTERS

LIST OF TABLES

TABLES

LIST OF FIGURES

FIGURES

CHAPTER 1

INTRODUCTION

Variable Stars are classified by two major groups, extrinsic and intrinsic variables, based on physical mechanisms that cause to change in their brightness over the time period [1]. Extrinsic variables identifies those stars whose light curve variability is caused by geometrical changes. Eclipsing binaries and rotating binaries belong to this class. Intrinsic variables, under other conditions, results from a series of physical changes occurring in the star. This branch itself divided into three major subclasses which are pulsating, eruptive and cataclysmic variables (CVs). The pulsating stars display a periodic increasing and decreasing in the size of their outer layers which lead to variations in their brightness and temperature. However, in the case of eruptive and cataclysmic variables, they often show sudden and violent explosions and flares which increase their luminosity dramatically. In this thesis, we discuss the X-ray properties of three selected cataclysmic variables (SS Aur, EY Cyg and TW Pic) using the archival X-ray observations provided by *XMM-Newton* and *SWIFT* space observatories. As an introduction, the first chapter gives a brief overview of previous studies about Cataclysmic Variables (CVs) such as classification, physical characteristics, accretion disk, outburst procedures and X-ray emission from these systems. In the second and third chapters, we present the methods and analysis of each system and discuss about them separately. Finally, in the fourth chapter, we give a summary of the results we obtained from this study.

1.1 Cataclysmic Variables

1.1.1 Discovery of Cataclysmic Variables

The first dwarf nova has been discovered by J. R. Hind in late 1855. It was the first very hot, blue star with a magnitude of nine in the Gemini constellation [2]. The newly discovered variable star "U Geminorum" (as its designated name) did not have the similar characteristics of the other variable stars which were known at that time. It was observed to brighten suddenly every few months. Late in middle of 20th century, astronomers discovered more similar systems by studying the light curves of each system i.e. a graph of light intensity received from an object over a period of time. Today, because of using the modern facilities in space science such as X-ray telescopes, the number of discovered CVs are growing. According to the catalogue provided by Downes et al. [3], there were 751 CVs known in 1993, the number changed to 1600 by 2006.

1.1.2 Definition and Classification

Cataclysmic variables (CVs) are interacting binary systems containing a compact star which in this case, a white dwarf accreting material from a low mass main sequence star (please see [4] for a review). In these systems, the primary star is a white dwarf (WD) as the compact star and the secondary star is a the main sequence donor from which material gets transferred via Roche Lobe overflow [5]. The orbital size of CVs are generally small and can be compared with the Earth-Moon set with a short orbital period of $<$ 15 h. Transferred material from donor star forms an accretion disk around the compact object, i.e., WD. In a wide energy band, from radio waves to gamma-rays, CVs can radiate electromagnetic spectra. Therefore, they have been studied widely using ground and space telescopes. The outer zones of accretion disk and its related secondary star are the main source of optical radiation. Ultraviolet emission which is important to study of the hot regions near the surface of WD as it comes from the inner parts of accretion disk. Despite other X-ray binary systems, the accretion disks of CVs are cool to emit large scale X-ray emission. The X-ray emission in the standard sense is expected from boundary layer that forms close to the white dwarf [4, 6]. It is because of shallowness of the potential well of the white dwarfs. Therefore, the accretion process from the disk to the white dwarf can be studied in the range of X-rays. Cvs also are one of the progenitors of supernova type Ia [7].

Cataclysmic Variables are divided into two major groups as Nonmagnetic CVs and Magnetic CVs. Nonmagnetic CVs are those systems where the white dwarf has a very small or no magnetic field and classified into subgroups of Classical Novae, Recurrent Novae, Dwarf Novae and Nova-like Variables depending on their eruptive behaviour. On the other side, in Magnetic CVs, the magnetic field of the white dwarf is strong enough to disrupt the structure of the accretion disc and the boundary layer (section 1.5.1). These systems also are divided to two subclasses, Polars and Intermediate Polars based on the magnetic field strength of the white dwarf. Though, the characteristics of CVs in each subgroup are different from the others, there is also overlap between them like some classical novae and dwarf novae which are intermediate polars, as well. These classifications are discussed in detail in the following subsections [8, 9].

1.1.2.1 Classical and Recurrent Novae

Classical Novae (CN) are cataclysmic variables that observed to brighten by 6 to 9 magnitudes during their outbursts (section 1.4.1). These systems have one single outburst. In addition, there is an inverse correlation between the eruption intensity and the fading rate of it. The brighter eruptions fade very fast about days to weeks, but the dimmer ones fade slowly (months to years). The mechanism responsible for these outbursts is the thermonuclear runaway of the Hydrogen-rich material accreted onto the surface of the white dwarf [10–12].

Recurrent Novae (RN) are the systems which undergo more than one nova eruption. The outbursts in these systems are cause of thermonuclear runaway on the white dwarf surface (see section 1.4.1 for more details). In RNe accretion occurs at a high rate onto a massive white dwarf (close to the Chandrasekhar mass; i.e.

T Pyx). In these systems, the recurrence period of outbursts does not follow a regular pattern and may vary from 10 to 100 years. RN systems are divided into two subclasses: long period and short period systems. *Long period* systems such as RS Oph, V745 Sco and T CrB have a period of a few hundred days. The secondary star in these systems is a red giant. *Short period* systems (T Pyx, U Sco and CI Aql) with a period of less than 2 days have a main sequence star as their donor star. ([13–16].

1.1.2.2 Dwarf Novae

Dwarf Novae (DNe) contain a white dwarf as its compact object and a late-type low mass main sequence star as its companion star orbiting around their center of mass with periods mostly between 80 min to 8 hours. In these systems, a continuous flow of matter is transferred to the Roche lobe of the WD. If the mass transfer rate is low the system is in quiescence. The quiescent state of DNe is altered every few weeks to tens of months by intense accretion flow called outburst. Outbursts are caused by a sudden increase in mass accretion rate through the accretion disc and are discussed in detail in (section 1.4.2). During the quiescent state accretion rate is in the range of 10^{-12} – 10^{-10} $M_{\odot}$ yr^{-1} ([6, 17] and references in them). All the three sources studied in this thesis are DNe in quiescence. Based on the morphology of the long term light curves, DNe can be divided to three different subgroups:

Z Camleopardalis stars (Z Cam) are known to exhibit a phenomenon called *standstill.* It is a state where the luminosity of the systems settles to a value $\sim$ 0.7 mag which is between the usual outburst and quiescent values. The standstill state occurs in those systems where the mass transfer rate from the secondary increases and may last from ten days to years. It is believed that during the standstill accretion rate from the secondary is higher than during the outbursts. Therefore, when the mass transfer rate from the secondary decreases, the system luminosity diminishes to the usual quiescent state [18–20].

SU Ursae Majoris stars (SU UMa) are short period (less than 2 hours) dwarf novae which occasionally exhibit superoutbursts. Superoutbursts are brighter outbursts with $\sim$ 0.7 magnitude which last 5 to 10 times longer than normal outbursts. The other characteristics that SU UMa stars show is *superhumps*. Superhumps are periodic hupms on the top of optical light curves of these systems and have periods slightly longer or shorter than the system's orbital period [21]. Superhumps result from the precession of the eccentric (or flexing) disk deformed by the tidal instability [22].

U Geminorium Stars (U Gem) generally are in their quiescent state and show normal outbursts between every ten to hundreds of days rather than exhibiting superoutbursts or standstills.

1.1.2.3 Nova-like Variables

Nova-like variables (NLs) is a subclass of CVs which are found to be mostly in high states with accretion rates $\sim 10^{-9}$ - 10^{-8} $M_{\odot}$ yr^{-1}. They may show variable accretion rates. Because of the high mass-transfer rate in these systems, the disc instability mechanism may be suppressed. They are well-known hard X-ray emitters [23]. Nova-like systems have subclasses like UX UMa, VY Scl and SW Sex [24]. *UX UMa* stars have a luminous accretion disk due to high mass-transfer rate and show strong and broad absorption lines in their optical spectra. *VY Scl* stars that also called "antidwarf novae" are the systems which occasionally dim by 3 – 5 magnitude in the optical. This downward transitions from steady high states into low states last from weeks to years. *SW Sex* stars are eclipsing systems with orbital periods of 3 – 4.5 hours which show single-peaked lines particularly He II [8, 25–27].

1.1.2.4 Polars

Polars (AM Her stars) have a white dwarf with a strong magnetic field (B > 10^7 Gauss) which prevents the accretion disk to form. Therefore, the material from the secondary is funnelled directly onto the magnetic poles of the white dwarf via an accretion stream (Fig 1.1). In this procedure, accreting material is entangled to the magnetic field and forced to move along the magnetic field

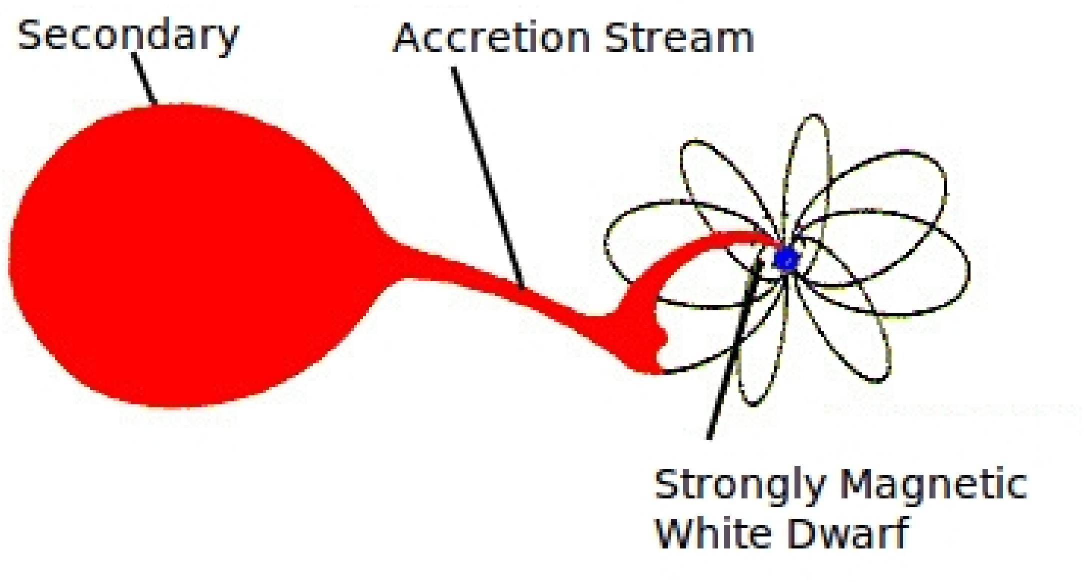

Figure 1.1: The geometry of Polars. The strong magnetic fields in Polars prevent an accretion disk to form and material is transferred directly from the secondary to the white dwarf poles via accretion stream. Adopted from https://heasarc.gsfc.nasa.gov/docs/objects/cvs/cvstext.html.

lines forming *accretion columns* (Fig 1.2) above the poles rather than boundary layer. The place that the material penetrate onto white dwarf is called *accretion spot* which is very hot. The accretion rate in polars is about 4×10^{16} – 2×10^{19} g/s [28] and according to Ritter and Kolb [29] catalogue the orbital period of these systems is longer than 77 min. In polars the spin period of the WD is equal to the orbital period of the system. It is due to the existence of the strong magnetic torque which locks the binary to synchronous rotation. In polars, falling material onto WD magnetic poles gets accelerated and reaches to supersonic velocities forming a strong stand-off shock close to the surface. In this region, the material is heated to temperatures around 10-40 keV and again cools as settles on the WD surface. The cooling process takes place through thermal bremsstrahlung by free electrons in the hot post shock region which produces hard X-ray emission. The origin of soft X-rays is the region close to the WD surface where the higher energy emission is reflected by the primary. While, the lower energy emission is absorbed or re-radiated as a blackbody radiation

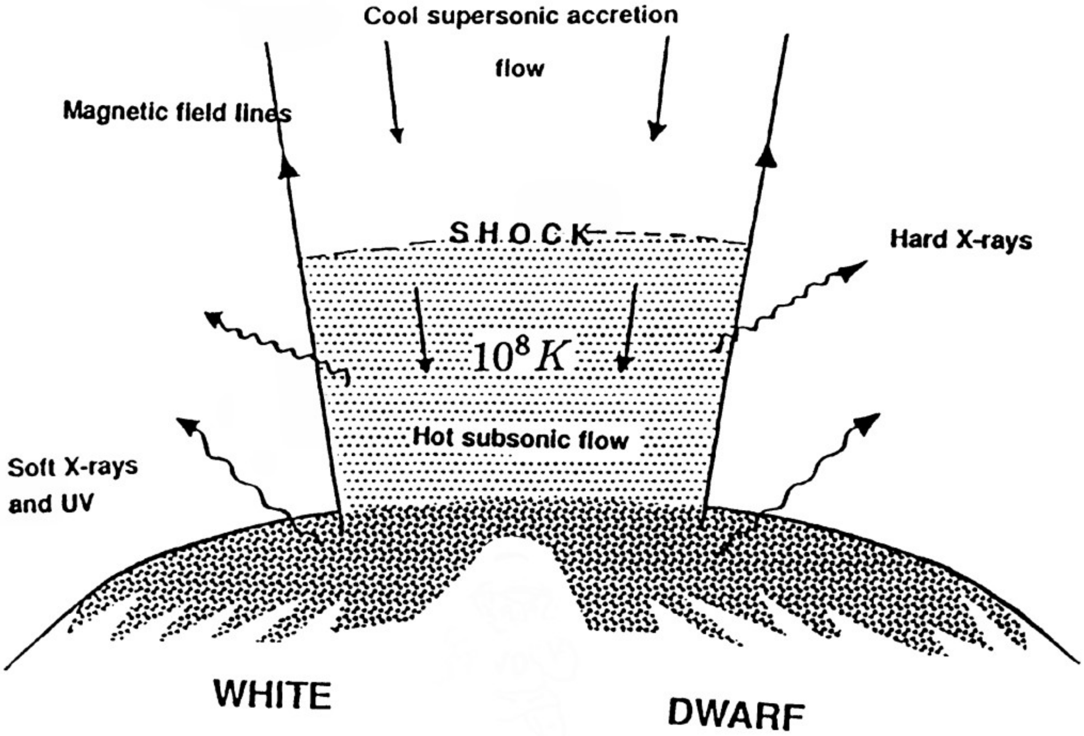

Figure 1.2: The accretion column in magnetic CVs. The figure shows the regions where soft and hard X-rays emerge from magnetic CVs. In these systems accreting material falls on the poles of white dwarfs (Adopted from Patterson (1994).

($kT_{BB} \sim 30$ eV) in the range of UV to soft X-ray. These systems also exhibit cyclotron emission at longer wavelengths from optical to infrared [30–32].

1.1.3 Intermediate Polars

In *Intermediate Polars (DQ Her)*, white dwarfs have a weaker magnetic field around $10^6 - 10^7$ G which is insufficient to create a huge magnetosphere. Smaller magnetosphere allows the accretion disk to form around the compact star however, the inner regions are disrupted by the magnetic fields. Therefore, the accretion flow channel onto the magnetic poles of the WD through magnetic field lines and creates *accretion curtains* [9, 32, 33]. See Fig 1.3 for more details

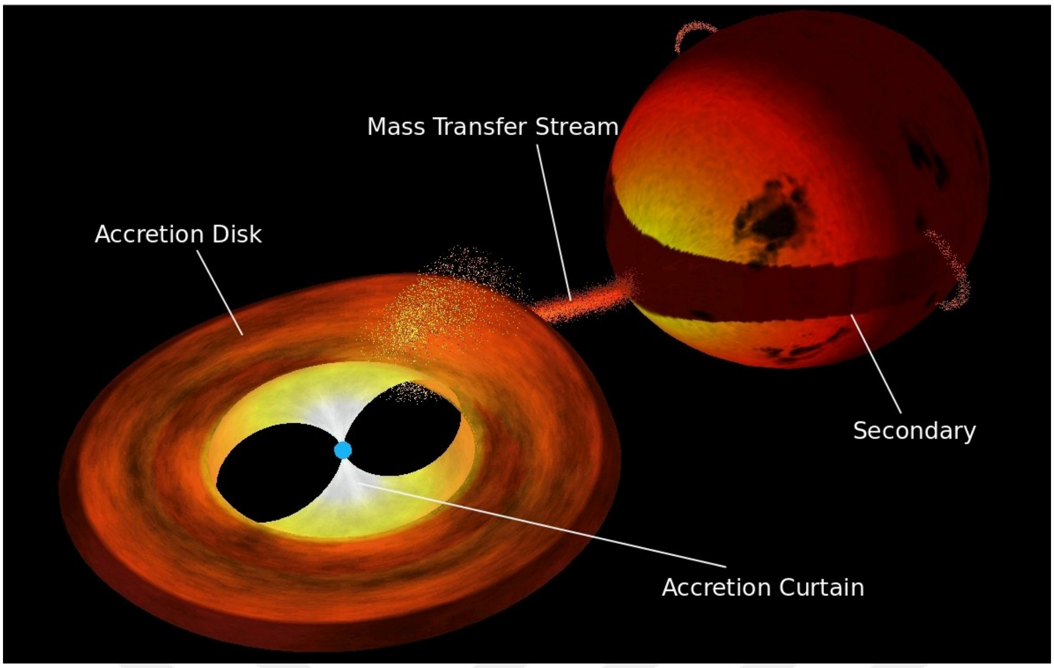

Figure 1.3: The geometry of Intermediate Polars. Inner regions of accretion disk in IPs are disrupted by the magnetic field of white dwarf. Thus, the material is transferred from inner disk to the white dwarf's surface through accretion curtains and columns. Credit: Andrew Beardmore, adapted from http://www.ing.iac.es/PR/press/v455.html.

on the geometry of IPs. The X-ray emitting process in IPs is very similar polars. The accreting material entangled in the WD magnetic field lines reaches high velocities higher than 3000 km/s and create a shock near the surface of the white dwarf with a temperature of about 10^8 K which needs to be cooled before settling on the white dwarf. This cooling procedure takes place via free-free interactions emitting hard X-rays [33]. Although, IPs have been noted for their hard X-ray emissions [34–36], some of them have been detected emitting blackbody radiation in softer X-rays [37–39]. Existence or nonexistence of blackbody component in these systems suggests that they can be divided into two groups, soft and hard systems. Evans and Hellier [40] suggested that the accretion polar caps are significantly blocked by the accretion curtains where this obscuration may be the reason for lacking of soft X-ray in some IPs.

Recent studies of IPs show that the hard X-ray emission is radiated from a multi-temperature plasma in the post-shock region. Therefore, the X-ray spectra of IPs can be well modeled by a composite model containing a multi-temperature plasma model together with a partially covering absorber. In the soft IPs, the soft X-ray emission can be taken into account by using a blackbody component with temperatures around few tens of eVs. Despite polars, the magnetic field of IPs is not that much strong to force the white dwarf to spin with the same rate of the binary system's orbital period. Therefore, intermediate polars are characterized by the existence of both orbital period P_{orb} and spin period P_{spin} where the spin period is much less than orbital period with a relation of P_{spin} /P_{orb} around 0.1 [41, 42]. Hence, there always exist two periodicities in the power spectra of IPs. This feature can be used to distinguish IPs from polars. Spin periods also give useful information of angular momentum flows in these systems. Generally, intermediate polars are known as the strongest hard X-ray (2-10 keV) emitters among CVs with a luminosity in the order of 10^{33} erg/s and an accretion rate of 10^{-10} – 10^{-8} $\mathrm{M}_{\odot}$ yr^{-1} [6, 36, 43].

1.2 The Geometry of Cataclysmic Variables

Kraft [44] by spectroscopic analysis of five U Gem type stars suggested that the secondary stars filling their Roche lobes transfer material from the primary's Roche lobe which are in contact at the inner Lagrangian point. Then the mass flow forms a ring or a disk around the primary, the white dwarf. Later, Warner [45] by photometric analysis of Z Cha proved that a disk exists around the white dwarf. In this section, We give a brief review of the geometry of Roche lobe, accretion disk, and orbital period in these systems.

1.2.1 Roche Lobe Geometry

Since CVs are binary systems which contain two bounded and orbiting masses, the relation between their components is well described by Kepler's third law,

$$a^3 = \frac{G}{4\pi^2}(M_{pri} + M_{sec})P_{orb}^2 \tag{1.1}$$

where G is the gravitational constant, M_{pri} is the white dwarf mass, M_{sec} is the mass of the secondary, $Porb$ is the orbital period of the system and a is the binary separation. For the values $M_{pri} = M_{sec} = \mathrm{M}_{\odot}$ and also the known range of orbital period of these systems which is P_{orb} = 1 - 16 hr, the binary separation can be obtained about 0.5-3 $\mathrm{R}_{\odot}$ ($\mathrm{R}_{\odot} \sim 7 \times 10^5$ km). This states that CVs are close binary systems. The total gravitational potential of the binary in a rotating system is given by

$$\Phi(\vec{R}) = -\frac{GM_{pri}}{|\vec{R} - \vec{R}_2|} - \frac{GM_{sec}}{|\vec{R} - \vec{R}_1|} - \frac{1}{2}(\vec{\omega} \times \vec{R})^2 \tag{1.2}$$

which is obtained by the summation of the gravitational potentials of each mass in addition of the effective potential of the centrifugal force. It defines the equipotential surfaces of the system that are known also as *Roche equipotentials* which depend only on the radial distance of the two components. Fig 1.4 shows the Roche equipotential surfaces in a CV. In the Eq(1.2) ω is the angular velocity of the binary, $\vec{R}$ is the radial vector of the center of mass -which is near the primary- and $\vec{R}_1$ and $\vec{R}_2$ are the position vectors of two components. The tear-drop-shaped regions, as shown in the Fig 1.4, bounded by a critical gravitational equipotential are called *Roche Lobes.*

The apexes of the Roche lobes are in contact at the inner Lagrangian point (L_1) i.g. which is an unstable point. When the secondary fills its Roche lobe the material flows into the primary's Roche lobe through the L_1 point [46, 47]. Since the Roche lobe of the primary is not filled, the transferred material finds a way to accrete on the primary's surface. Those binaries like CVs in which one of the stars filled its Roche lobe but the other one not, are called *semi-detached* systems. In *detached* systems both stars are in their places and none of the Roche lobes are filled. Evolving the secondary therefore, the expansion of it fills the Roche lobe allowing material to transfer steadily and continuously. The concept of angular momentum is in the way which the binary system loses its angular momentum during a steady mass accretion. Losing angular momentum reduces the size of Roche lobe which keeps the secondary to be in contact with it and mass accretion goes on.

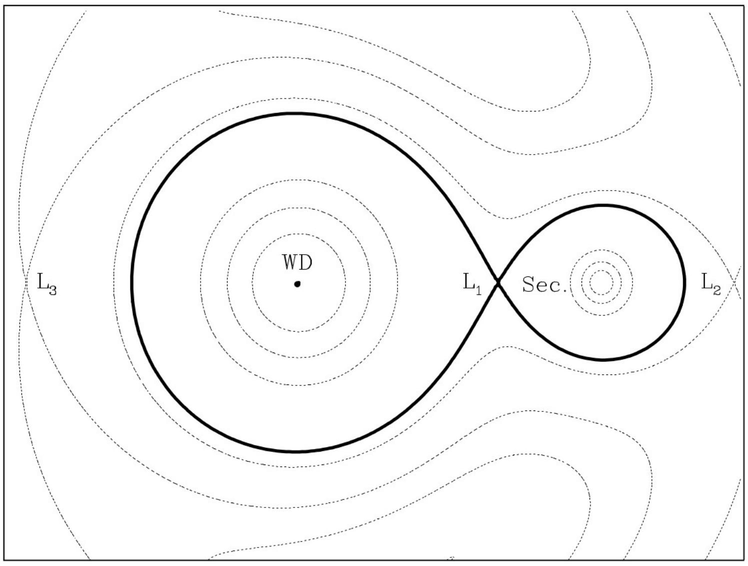

Figure 1.4: The Roche equipotential surfaces and Lagrangian points in a CV with $M_{sec}/M_{WD} = 0.2$. The bold line indicates the Roche lobes of each component which are in contact at the inner Lagrangian point L1. Once the secondary filled its Roche lobe, material is transferred towards the WD through L1. Adopted from Matthias Schreiber (2001) doctoral thesis.

There are two main mechanisms responsible for the loss of angular momentum from CVs: gravitational radiation and magnetic braking [48]. Gravitational radiation (Gravitational Wave) firstly predicted by Albert Einstein in 1916 based on his theory of general relativity. Gravitational radiation (Gravitational Waves) predicted by Albert Einstein in 1916 [49] and discovered in 2016 (LIGO, [50]), results from repetitive orbiting of the binary stars in a shrinking orbit that provides the necessary energy.

The stellar wind ejected from the secondary plays the main role. Stellar wind is an outflow of ionized particles from the atmosphere of stars e.g., like the solar wind which causes Aurora phenomenon when it passes through the Earth. In CVs, the secondary has a stronger magnetic field than a single star. It is because of the presence of tidal force which shorten the orbital period and make the secondary rotate rapidly. Therefore, the ionized particles in the wind along the magnetic field lines leave the system while taking angular momentum with them. Hence, the binary compensate the lost angular momentum by shrinking the orbit [48, 51].

1.2.2 Orbital Period

Most of the CVs which contain a Roche lobe-filling main sequence star as their secondary and a white dwarf as primary have an orbital period between 78 min to 10 hours. There is a shortage of systems with periods in the range 2 and 3 hours which is referred as the *period gap.* The period gap is the stage which the system is switching from magnetic breaking [48] with a high accretion rate and a longer period of $P_{orb} > 3h$ to a lower accretion rate in which the mass transfer is driven by gravitational radiation with periods < 2 h. This period gap is maintained by thermal timescale of the secondary star.

1.3 Accretion in Nonmagnetic Systems

The accreting material transferring to the white dwarf through L_1 point moves with the sound speed about 10 km/s. In addition, the binary system is orbiting around its center of mass with an orbital velocity of about 100 km/s. These two perpendicular velocities do not allow the material fall directly onto the white dwarf but, make it spiral around the primary. By dissipating energy, the material settles into a circular orbit of the lowest energy forming a ring. In addition, based on the conservation of angular momentum, the material has the same angular momentum obtained in L_1 point, therefore, it needs to orbit at a certain radius that maintains its angular momentum. This radius is called the *Circulisation Radius* [52]. According to the Kepler's law material in the inner orbits moves faster than those in the outer parts.

The difference between the velocities of the material in inner and outer parts of the ring leads to friction and turbulence which heat the gas to radiate energy. By losing energy, material moves to smaller orbit. The torque between the rings in the disk allows the material to be transferred in the disk. Consequently, the outer orbit material should move to larger orbits to keep the angular momentum conservation. It results that the ring spreads out and creates a thin disk that is known as an accretion disk (Fig 1.5). This spreading will continue until the inner boundary of the disk reaches the white dwarf. Thus, the material from

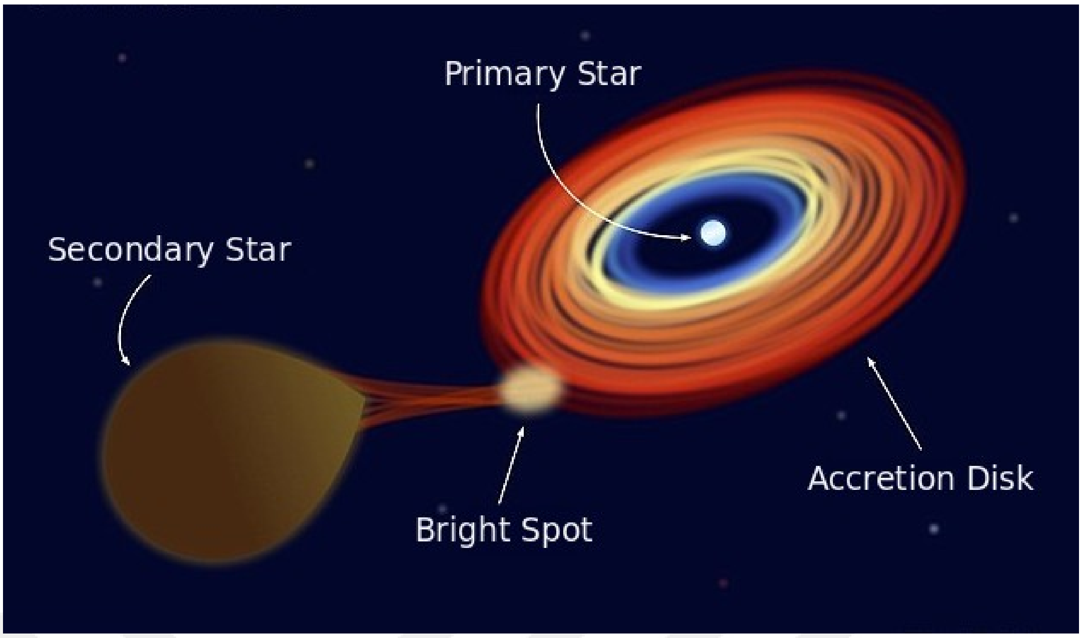

Figure 1.5: The figure illustrates the different parts of a nonmagnetic CVs and how mass flow from secondary forms a disk arounf the white dwarf. Credit: Rene Breton, adopted from https://phys.org/news/2016-05-stellar-cannibalism-star-brown-dwarf.html.

the secondary star accretes on the white dwarf's surface through the innermost region of the disc which is called the *boundary layer* (section 1.5.1). The outer edge also sets its radius after undergoing tidal interactions with the secondary [53].

The thin disk theory which was developed by Shakura and Sunyaev [54], Lynden-Bell and Pringle [55] assumes that the accretion flow is steady and geometrically thin where the angular momentum transfers to the viscosity which let the disk to radially exchange blobs of material. To explain that how the viscosity governing the material through the disk, Shakura and Sunyaev [54] parametrised the viscosity in terms of turbulent eddies by introducing the α-prescription as

$$\nu = \alpha c_s H \tag{1.3}$$

where α is a constant between 0 to 1, H is the height of the disk and c_s is the sound speed. Actually, they assume that the H is the upper limit for the size of the eddies. In addition, as gas molecules move with speeds near c_s, eddies in the disk can speed up material at most up to the speed of sound. The first place where the mass stream from the secondary impact the accretion disk is called the *bright spot.* This supersonic encounter converts large amounts of the kinetic energy of the flow to heat and radiates in optical and UV regimes (about 30 % of total brightness of the system). The temperature distribution in the disk depends on the radius and can be measured from about 5000 K at the outer radius to about 100000 K in the inner disk near the white dwarf [8]. Accretion disk can be studied in a large energy band from IR to X-rays.

1.4 Outburst Behaviour

Outbursts are one of the most remarkable features of CVs and regarding their mechanisms can be divided into two subclasses as *classical and recurrent nova outbursts* and *dwarf nova outbursts.* Classical nova outbursts are due to explosive ignition of H-rich envelopes on the surface of the WD. While dwarf nova outbursts are due to disk instabilities. During outburst, the system brightens dramatically allowing scientists to study different characteristics of the system. These mechanisms are going to be discussed in the following sections.

1.4.1 Classical Nova Outburst

Classical nova outbursts occur as a result of thermonuclear runaway (TNR) due to the accretion of hydrogen-rich material onto a the surface of the white dwarfs in CVs. Though, white dwarfs burn most of their hydrogen out during their stellar evolution, the accreting material forms a layer of mostly fresh hydrogen on the surface of them. This provides the circumstances of restarting nuclear reactions. Continuing of this procedure over long periods of time makes the layer more dense. Therefore, the pressure in the bottom of the layer increases and the electrons from the ionised hydrogen become degenerate. By accreting more material temperature increases and hydrogen fusion starts consequently. However, the degeneracy pressure prevent the material to expand till the temperature at the layer reaches the temperatures $\sim 10^7$ K [56]. At this point the

TNR speeds up and temperature increases rapidly. The β-unstable nuclei goes up to outer layers through convection. Energy dumped in the outer layers causes these layers to expand.

During the outburst the some layer of accreted hydrogen will be ejected from the surface of the white dwarf and will radiate in the range of 10^{32} – 10^{35} erg s^{-1} as a result of ejecta interactions. The velocities measured for the ejecta is in order of 10^3 km s^{-1} [56]. The average of the ejected mass was estimated to be 2 $\times$ 10^{-4} $M_\odot$ and contains metal-enriched gas which is a source of heavy elements for the interstellar medium [57, 58]. According to the theoretical calculations it takes about 10^4 to 10^5 years that the system undergoes an outburst again. The outburst increases the brightness of the system by $\Delta m = 9 - 10$ magnitudes in the optical wavelength. The outburst duration takes from weeks to several years.

1.4.2 Dwarf Nova Outburst

Unlike CN outbursts that the eruption process takes place in the surface of white dwarf, dwarf nova outburst procedure begins from the accretion disk. The mechanism responsible for dwarf novae outbursts is the thermal-viscous instabilities in accretion disks [59]. It occurs when the mass transfer rate from the secondary exceeds the accretion rate onto the white dwarf. The high rate transferred material cannot be transported through the disk towards the WD because of viscous interactions. By accumulating of material in the disk the density increases and the temperature reciprocally rises to 10^4 K. This is the temperature in which hydrogen would be ionized. Due to the ionization the temperature increases dramatically to 3 $\times$ 10^4 K and the disk becomes thermally unstable. Critical viscosity is reached now and the excess material is driven away by the disk towards the white dwarf resulting an outburst. In order to keep angular momentum constant, the disk spreads some of the material outward which expands the disk radially. During the outburst, the luminosity of the system is increased by a magnitude of 2 – 6 and lasts from few days to about more than a month. The recurrence times in these systems varies from few days to tens of years. Moreover, the outbursts of the same system can be different in magnitude and duration. After outburst, the system returns to its quiescent state till the next outburst creating a cycle which is called *outburst cycle* [8, 9, 60].

1.5 X-Rays From Nonmagnetic Systems

The first signs of X-ray emissions radiated from cataclysmic variables were detected through observations of EX Hya obtained by Uhuru observatory [61]. After that, many X-ray observations had been performed to scan space to detect X-ray radiation from CVs. Consequently, soft X-ray emission was detected by a rocket flight which had a X-ray detector (0.15 - 0.28 keV) on board. The soft X-rays were emitted from SS Cyg which is brightest dwarf novae in the sky [62]. Later, Heise et al. [63] detected hard X-ray emission from the same source (SS Cyg). Since then, further developments in space technologies and also launching new strong X-ray observatories like *XMM-Newton*, *CHANDRA* and *SWIFT* let scientists to wider their understanding of X-ray emission from CVs. In the following section, we discuss about the origin and also mechanism of X-ray emission from non-magnetic CVs.

1.5.1 Boundary Layer

The matter in the inner disk has initially a Keplerian velocity which is almost 3000 km/s. In order to accrete onto the WD which rotates at considerably lower velocities, the accreting material should lose its rotational kinetic energy and be slowed down [6, 64]. This procedure takes place in the region very close to the surface of the WD which is known as boundary layer. In the other words, the Boundary layer is radially between the accretion disk and central compact object. Generally, the accretion disk is expected to emit half of the available gravitational potential energy mostly in optical and ultraviolet (UV) wavelengths while the other half comes from the boundary layer mostly in the extreme ultraviolet (EUV) and X-ray at the range of 10^{29} – 10^{32} erg s^{-1} for dwarf novae in quiescence ($L_{disk} \simeq L_{BL} \simeq GM_{*}\dot{M}/2R_{*}$, where M_{*} and R_{*} are

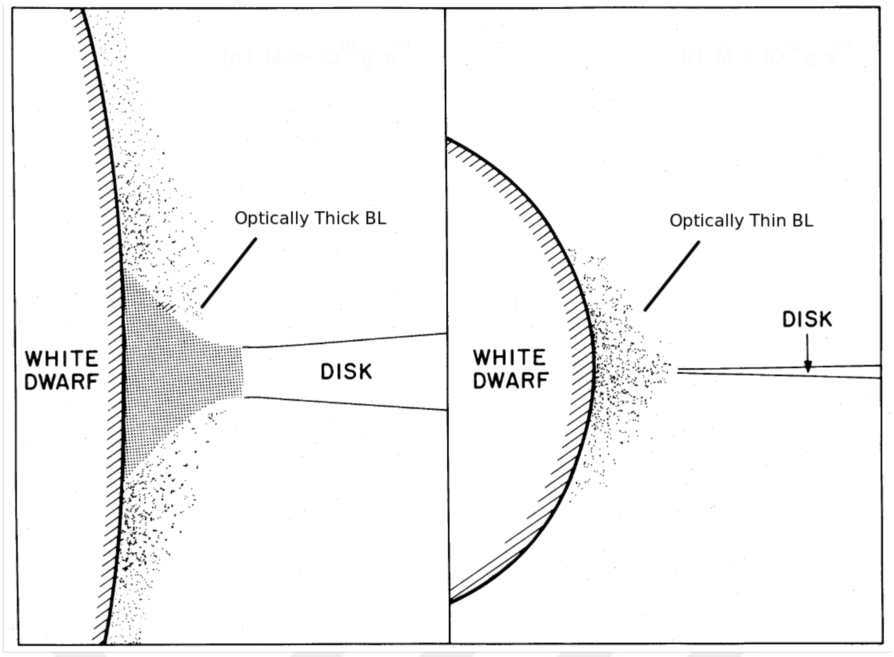

Figure 1.6: The boundary layer in nonmagnetic CVs. The left picture shows the system in high accretion rate state ($\dot{M} > \dot{M}_{crit}$) in which the boundary layer is optically thick and the right picture shows the system in low accretion rate ($\dot{M} < \dot{M}_{crit}$) where the boundary layer is optically thin. Adopted from Patterson and Raymond [65].

the mass and radius of the compact star) [17, 66–70].

As X-ray emission can be expected from other structures, how can we be sure that the X-rays coming from CVs are originated in the boundary layer rather than the corona of the secondary star or the hot spot? There are some parameters which ensures that the BL is the best candidate for X-rays like X-ray luminosity and bremsstrahlung temperature. The X-ray luminosities radiated from single secondary-like stars are less than the X-ray luminosities observed in CVs. In addition, the coronal spectrum shows smaller bremsstrahlung temperatures in comparison with those in CVs. For the hot spots, it can be explained that the temperature parameter the T_{max} of hot spots is much smaller than the temperatures measured in X-ray sources.

There are also systems where the X-ray luminosities are dramatically lower than expected especially the systems with high mass accretion rate [71, 72]. This effect is called "missing boundary layer problem" [73]. According to van Teeseling and Verbunt [74] the majority of the energy that is expected to be emitted as X-ray fluxes is consumed in a non-radiative way such as driving an accretion disk wind.

However, there are other explanations such as coronal siphon flows [75], inner disk disruptions by rapid rotating WD [76] or magnetic fields [77] or irradiation from a hot WD [28]. Balman et al. [23] have suggested that this may be a result of hot flows that have ADAF-like properties in the inner accretion disk of high-state nonmagnetic systems.

The energy of the emitted X-ray depends on the optical depth (thickness) of the boundary layer. Also, the optical depth itself is in connection with the mass accretion rate. Therefore, in low accretion rate CVs where the accretion rate is smaller than the critical mass accretion rate $\dot{M}_{crit} \sim 10^{16}$ gs^{-1} the boundary layer will be optically thin (Fig 1.6-right). In this state which is known as the quiescent state, optically thin boundary layer radiates mostly in hard X-rays at the temperatures of $\sim 10^{7.5} - 10^{8.5}$ K [72, 78–81].

Conversely, in high accretion rate ($\dot{M} > \dot{M}_{crit}$) like dwarf novae in outburst, the boundary layer becomes optically thick (Fig 1.6-left). Unlike the optically thin boundary layer, in an optically thick boundary layer the emission diffuses through the region and the hard X-rays are suppressed. Thus, only extreme UV and soft X-ray emissions are observed in these systems [70]. The optically thick boundary layer allows the material to cool efficiently. Therefore, the boundary layer heated up to the temperatures about 10^5 K emits blackbody radiation [69, 70, 78].

1.5.2 X-ray Spectral and Temporal Properties

Before the developments in X-ray observatories the spectra on nonmagnetic CVs were consistent with a single temperature bremsstrahlung radiation in the range 2-20 keV e.g. X-ray emission detected by EXOSAT [82]. This is because of poor statistics and resolutions of observations. However, as X-ray facilities got improved and high resolution data were produced, X-ray spectra showed more complex features. During the analysis of the Ginga spectrum of SS Cyg they found Fe Kα (6.7 keV) which was not consistent with the plasma temperature of 18 keV. To explain this inconsistency, they used two bremsstrahlung models at different temperatures [83]. These results confirmed that the previous belief of a single temperature plasma boundary layer is not acceptable. Further X-ray observations of CVs indicate that the material settling on the white dwarf's surface is an isobaric cooling flow plasma with a temperature distribution in the range of 6 – 55 keV [17]. Therefore, X-ray spectra of CVs can be best modeled with multi-temperature thermal plasma models [17, 43, 64, 68, 84–86].

Non-magnetic CVs generally show emission line of Fe Kα which can be resolved into three separate lines: 6.4 keV fluorescent line, He-like Fe XXV line in 6.67 keV and H-like Fe XXVI line in 6.97 keV. The Fe XXV and Fe XXVI lines emanate from hot plasma with a temperature range of $10^8 - 10^9$ K. The fluorescent line is believed to emerge due to X-ray reflection (scattering) from the white dwarf's surface or the inner part of accretion disk. This was first realized from ASCA observation of SS CYG by Done and Osborne [87]. Although reflection component can reveal more information about the boundary layer and areas very close to the white dwarf, however, instrumental factors such as small effective area and low sensitivity at higher energies make it hard to investigate. Studying of Fe XXV and XXVI lines can also provide useful information about temperature, density and ionization state of the radiating plasma. Other elements can be detected in X-ray spectra such as O, N, Mg, Si and Ne which are determined by emission line analysis in proportion to solar abundances.

X-ray light curves of the non-magnetic CVs enable us to study the orbital eclipses that provide important information about the location and size of the region emitting X-rays. Eclipses occur when the emitting region is obscured, therefore, they highly depend on the inclination of the system. In some dwarf novae, X-ray eclipses are shorter than the optical eclipses [88]. In addition, in the X-ray light curves, there is a delay in rise to outburst with regards to the optical light curves of several hours upto a day [75].

CHAPTER 2

XMM-NEWTON OBSERVATIONS

2.1 Observatory and Instruments

The X-ray Multi-Mirror Mission, *XMM-Newton* satellite [89], is a X-ray space observatory which is operated by the European Space Agency (ESA; Fig. 2.1). It was launched on December 10, 1999 by an Ariane 5 and has the largest effective area of any other X-ray telescopes. *XMM-Newton* satellite carries three medium spectral resolution X-ray imaging detectors each with an European Photon Imaging Camera (EPIC) at the focus. Two of them have a multi-object spectrometer (MOS) CCDs [90], which are operating in small-window mode, and the other is in full-frame mode (pn) [91]. The MOS1 and MOS2 have made by 7 CCDs with a pixel size of 40 μm while pn includes 12 CCDs with 150 μm of pixel size. The EPIC cameras are designed to observe X-rays in the energy range of 0.2 – 15.0 keV with a 30 arcminutes of field of view. In addition, there is a 0.3 m optical/UV imaging telescope on-board with a field of view of 17 arcminutes. The optical monitor (OM) is a photon-counting instrument which enables simultaneous X-ray and optical/UV observations [92]. The wavelength coverage of the optical monitoring camera is in the range of 170 nm – 650 nm. *XMM-Newton* also contains a high resolution spectrometer called Reflecting Grating Spectrometer (RGS) [93]. It is a high-resolution spectrometer which is operating simultaneously with EPIC detectors in the range of 0.4 – 2.5 keV.

2.2 Data and Observation

The archival *XMM-Newton* data were reduced and analyzed using the *XMM-Newton* Science Analysis System SAS version 11.0.0 and 14.0.0 and with the latest available calibration files. In order to use well-calibrated and cleaned

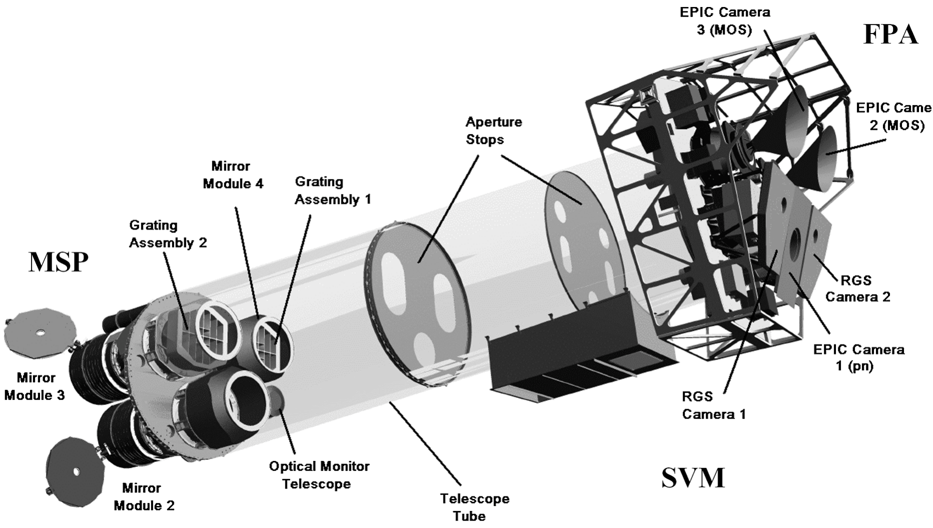

Figure 2.1: Schematics for *XMM-Newton* observatory and its on-board instruments. Figure is adopted from [94].

data, the standard filtering expressions were applied to all observations. For the pn data, single and double pixel events with PATTERN$\leqslant$4 and #XMMEA_EP and for the MOS, PATTERN$\leqslant$12 and #XMMEA_EM were used. In addition, we used FLAG = 0 to exclude bad pixels and events at CCD edges. All observations were checked in the case of pile-up contamination.

SS Aur was observed by *XMM-Newton* observatory on 07 April 2008 (Observation ID 0502640201) when the system was in quiescence for 51 ks. We analyzed the archival data extracting the X-ray spectra and light curves using circular regions of 27.5, 30 and 32.5 arcsec radius on pn, MOS1, and MOS2, respectively. The background spectra and light curves, likewise, were extracted from a source-free region on the same chip for pn and on the suitable chips for MOS1 and MOS2. To remove the flare activities, all three light curves were cut off after time = 3.9×10^4 s using a time filter in the light curve extraction. The OM data was configured in the fast mode using the OMFCHAIN with time bin size of 0.5 s. The OM data provided us ten exposures with a total duration of 37.2 ks through the UVW1 filter (240-340 nm) and two exposures of 7.7 ks in the B filter (400-500 nm).

EY Cyg, as well as SS Aur, was observed with the same satellite on 23 April 2007 (Observation ID 0400670101) with 45 ks of exposure time. The source and background regions were extracted from the same chip with the radii of 18 (pn), 18.5 (MOS1) and 17.5 (MOS2) arcsec. The same procedure was done to extract EPIC X-ray spectra and light curves. The OM observations were not performed for this source. All light curves were background subtracted and barycentric-correction was performed.

2.3 Analysis and Results

2.3.1 SS Aur

SS Aurigae is a dwarf novae of the U Geminorum type stars [95] with an orbital period of 263.232 minutes derived from variation of Hα emission lines and with the ephemeris T_0 = 2446439.754 [96]. Since, they could not find the precise time for conjunction for the system, they took the T_0=t_0(a=9 Å) where a is the half separation of Gaussian bandpass and t_0 is the time of conjunction of the emission line source. The emission line sources are expected to be in the inner regions of the disk. The visual magnitudes of the system during quiescent and outburst are $\sim$ 14.5 and $\sim$ 10.5 mag, respectively [97]. The system parameters are given in Table 2.1. The system is located at the distance of $\sim$ 201 pc [98]. Shafter [99] showed that the mass of the primary in this system is about 1.08 $\pm$ 0.40 $M_\odot$, while its secondary estimated to have a mass of 0.39 $\pm$ 0.02 $M_\odot$. The inclination of the system is $i = 38° \pm 16°$. However, Lake and Sion [97] obtained different values for the parameters by analysing the *IUE* far-UV archival spectra of the system. They found out that the SS Aur has a hot white dwarf with T_{eff} = 30,000 K, M_{wd} = 1.03 $M_\odot$, i = 41°, and $\dot{M}$ = 10^{-10} $M_\odot$ yr^{-1}. Later, SS Aur has been studied in the far-ultra violet domain by Sion et al. [100]. They used a model consisting a white dwarf atmosphere and an accretion belt to fit the Far Ultraviolet Spectroscopic Explorer (FUSE) spectra of the system which yielded T_{eff} = 33,000 K. In the same year, Harrison et al. [101] showed that the inclination of the system is 40 $\pm$ 7 deg.

In the X-ray domain, Byckling et al. [102] revealed a spectral analysis of SS Aur using Suzaku/XIS archival data which have been obtained in March, 2008. In the

Table 2.1: System Physical Parameters of SS Aur

Parameter	Unit	SS Aur
M_{wd}	$M_{\odot}$	1.03[a]
M_{2nd}	$M_{\odot}$	0.39 ± 0.02[b]
i	deg	40 ± 7[c] 6
P	day	0.1828[d]
T_0	HJD	2446439.754[d]
d	pc	201[e]
V_{min}		14.5[a]
V_{max}		10.5[a]

[a]Lake and Sion [97]; [b]Shafter [99]; [c]Harrison et al. [101]; [d]Shafter and Harkness [96]; [e]Harrison et al. [98]

time, the system was in its quiescent state. They used photoelectric absorption (*wabs*) together with a cooling flow model (MKCFLOW) and a 6.4-keV Gaussian line which yielded a χ^2_ν of 0.95. Their model computed the hydrogen column density $N_H = 3.3 \times 10^{20}$ cm^{-2} which is lower (about one order of magnitude) than the N_H we used for our analysis ($N_H = 2.3 \times 10^{21}$ cm^{-2}). Consequently, they derived unabsorbed flux and luminosity in an energy band of 0.01-100.0 keV from the cooling flow model ($kT_{max} = 23.47$ keV) of 7.1×10^{-12} erg s^{-1} cm^{-2} and 2.39×10^{31} erg s^{-1}, respectively.

2.3.1.1 Timing Analysis

To carry out the timing analysis we applied the solar system barycentric correction to correct the event times. Using the same regions previously described, the standard SAS task EVSELECT was used to extract three light curves from the data sets of all three X-ray CCDs with a bin size of 0.1 s. Fig. 2.2-top shows the unfolded background-subtracted X-ray light curves. Plotting and folding procedure were carried out with the XRONOS task LCURVE. The light curves show the source in the quiescent state. In order to compare X-ray timing results directly with the OM time series, we also extracted the OM light curves using the standard SAS procedure OMFCHAIN for the extracting and reduction of the OM data. The OM light curves were produced from barycenter-corrected time series in two energy filters UVW1 (240-340 nm) and B (400-500 nm) with 0.5 s bin size. Fig. 2.2-bottom shows the two light curves of filter UVW1 and filter B.

To study the variation of the X-ray and optical light curves, we folded EPIC and OM light curves over the orbital period of the system using 10 phase bin and norm=0 using XRONOS task *efold*. For SS Aur, we assumed 0.1828 ± 0.001 days as orbital period that was derived from Hα emission line and the ephemeris T_0(HJD) = 2446439.754 reported by Shafter and Harkness [96]. Fig. 2.3 shows the folded light curves over the orbital period. The maximum and minimum phases of the folded light curve extracted from UVW1 filter mostly match the Shafter and Harkness [96] radial-velocity curve derived by Hα variations. The folded optical light curves of B-band and the UVW1 over the orbital period show phase shifts in minima and maxima with regard to the folded X-ray light curves. In non-magnetic CVs, a hotspot at the accretion impact zone may be the responsible for these phase shifts.

In order to investigate the physical state near the white dwarf, analysis of the rapid variability in the source flux could be helpful. Therefore, we extracted the power spectral density (PSD) to search for periodicities or coherent Quasi-Periodic Oscillations (QPOs) of the source. For this purpose, we used XRONOS task POWSPEC which converts a time domain light curve to a frequency domain power spectrum via Fourier Transformation (FT). For this, we used the total duration of light curves with a minimum time bin of 0.1 s (EPIC) and (0.5 s for OM) for having one interval in the related plot. In addition, we used the Leahy normalization for the power spectra [103]. The power spectra of the both X-ray and optical light curves were analysed. We did not detect the orbital period of the system with the frequency of 6.33×10^{-5} in the power spectra. No significant QPO was seen in SS Aur PSDs (Fig. 2.4). There are some high peaks in the PSDs, but they do not show steady frequencies and the peak structures changing with binning. The PSDs suggesting high levels of red noise are produced by low frequency aperiodic intrinsic variability of the source [104] and can create the

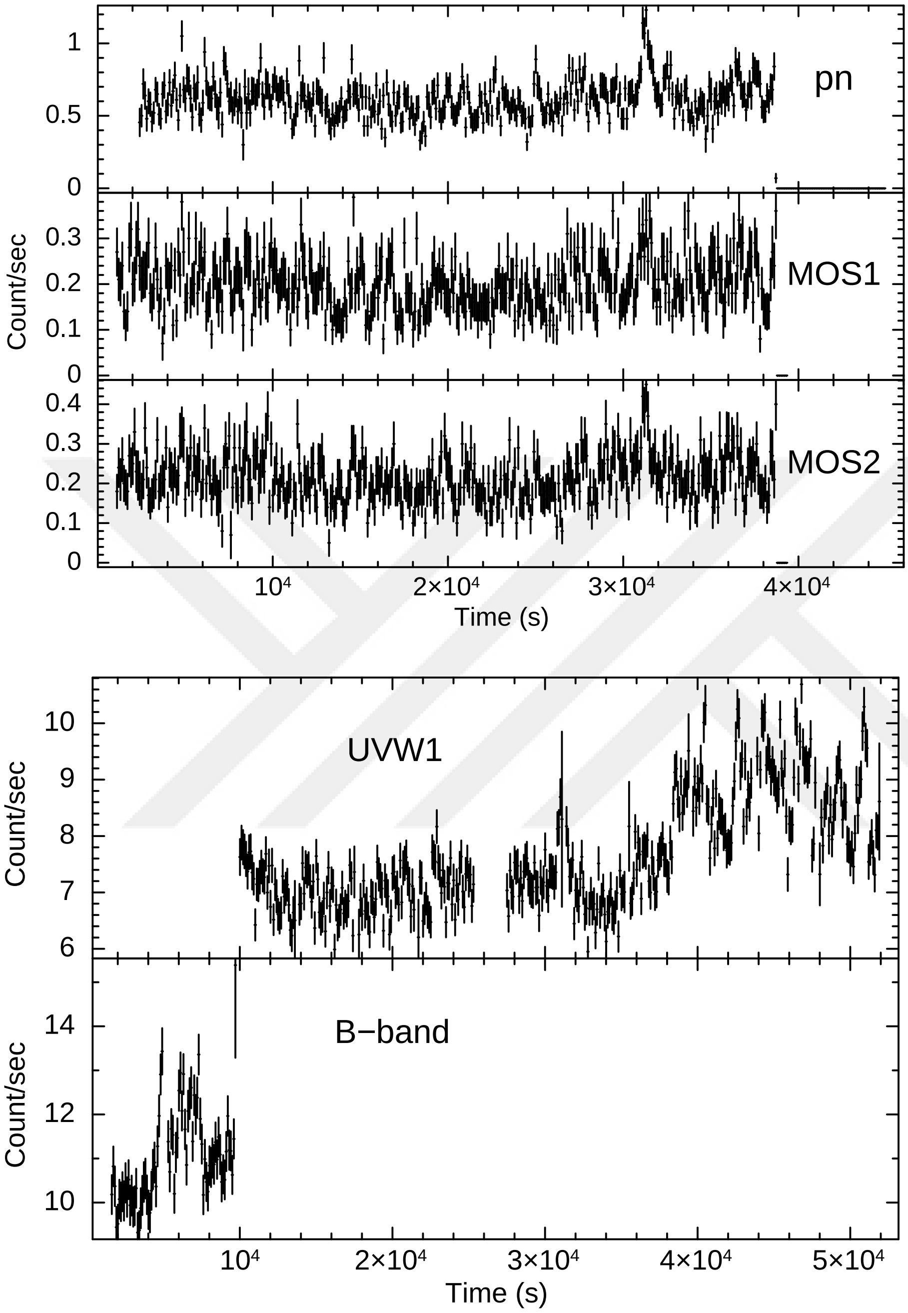

Figure 2.2: The *XMM-Newton* light curves of SS Aur derived from EPIC (top) and OM (buttom) data with the time bin size of 100 s.

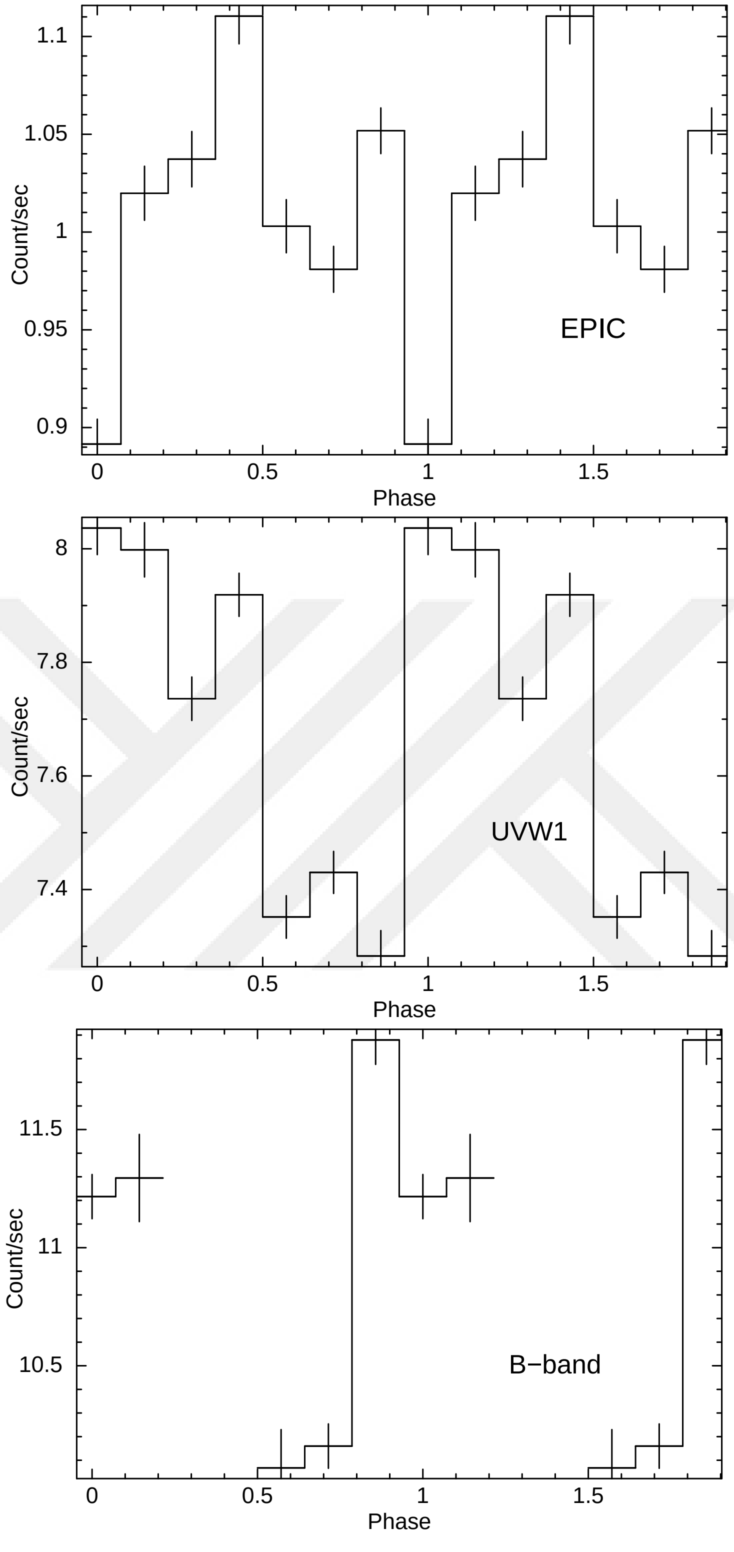

Figure 2.3: The *XMM-Newton* EPIC light curves (pn+MOS1+MOS2) (top) and OM light curves of SS Aur folded over the orbital period of 263.232 minutes for X-ray (top), UVW1-filter (middle) and B-filter (bottom). We used T_0(HJD) = 2446439.754 reported by Shafter and Harkness [96].

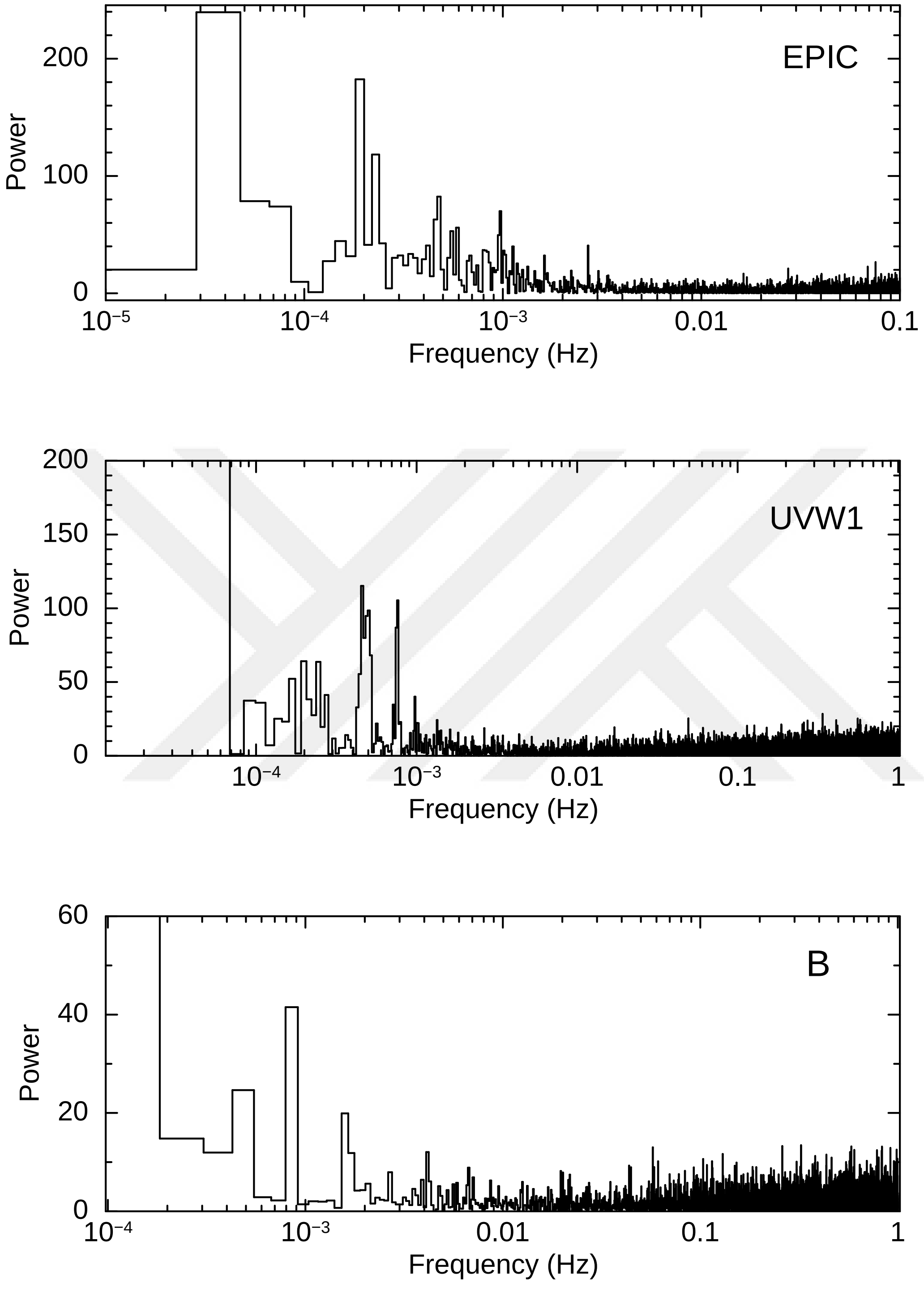

Figure 2.4: Power spectral density obtained from averaged power spectra of the combined EPIC light curves (top) UV light curve (middle) and optical light curve (bottom).

false peaks in the PSD.

2.3.1.2 Spectral Analysis

We reduced the event files and applied the SAS task ESPECGET in order to drive the X-ray spectrum for EPIC pn ($\sim$ 0.7 count/s), EPIC MOS1 ($\sim$ 0.2 count/s) and EPIC MOS2 ($\sim$ 0.2 count/s) together with the appropriate response matrices and ancillary files. In addition, for increasing the signal to noise ratio and achieve good statistics, we grouped the spectra to have at least 30 (MOS1 and MOS2) and 70 (pn) counts in each energy bin. The spectral fitting was simultaneously performed for all three EPIC spectra using XSPEC version 12.8.0 [105] in the energy band of 0.3-9.8 keV. A constant factor was added to the fit to account for cross-calibration normalization between EPIC instruments. We fitted the spectra with proper plasma emission models which are explained in detail below. The spectral parameters are given in Table 2.2. The spectra of pn, MOS1 and MOS2 are shown in the Fig. 2.5-bottom together with the best-fit model.

In nonmagnetic CVs, as expected, the accreting material ($kT_{max} \sim$ 10-50.0 keV) should be cooled before settling on to the WD surface through the boundary layer. The structure of the boundary layer is not fully understood yet. However, we can discuss about the general characteristics of the emission originated in it. The settling material onto the white dwarf surface covers a temperature distribution of hot optically thin cooling gas flow [43, 64, 68, 84–86]. Hence, in a simple way, the spectra of such systems are well modeled with an isobaric cooling flow which is a multi-temperature distribution of plasma characterized by an emission measure following a power-law temperature dependency ($dEM = (T/T_{max})^{\alpha-1} \mathrm{d}T/T_{max}$) like MKCFLOW and CEVMKL (built from the mekal code [106]).

In our first attempt to fit the spectra within XSPEC (see the XSPEC user's manual for a comprehensive description), we used *tbabs* (which calculates the cross-section for X-ray absorption by the interstellar medium due to gas, grain, and molecules in the ISM; see Wilms et al. [107] for more details) model to account for the absorption through the interstellar medium together with a multi-temperature plasma emission model (CEVMKL) as expected from low accretion rate quiescent dwarf novae. We fixed the value of neutral hydrogen column density at 0.23×10^{22} atoms cm^{-2} which we obtained from nhtot[1] (Willingale et al. [108]).

The composite model gave a poor fit with an unacceptable reduced χ^2 value of 3.6 and the existence of soft excess was clear (see Fig. 2.5-top). In order to improve the fit, we added a blackbody model (*bbody*; $A(E)$=$K\times$ $8.0525E^{dE}/(kT)^4$ $[exp(E/kT) - 1]$, where kT is the temperature (keV) and K is normalizarion $(\frac{L_{39}}{D_{10}^2})$, where L_{39} is the source luminosity in units of 10^{39} erg s^{-1}, D_{10} is the distance to the source in units of 10 kpc.)[2] and obtained a fit of $\chi^2_\nu = 1.95$ (dof 592). Though, blackbody model fitted the excess, the χ^2_ν was not still good. We, then added a power law model (*powerlaw*; $A(E) = KE^{-\alpha}$, where α is photon index of power law (dimensionless) and K is the normalization (photons/keV/cm^2/s at 1 keV))[3] which gave us an improved fit with a better $\chi^2_\nu = 1.18$ (dof 590). We then allowed the Oxygen and Iron to vary from solar abundances, and obtained a best fit with reduced χ^2 of 1.05 (dof 588). Finally, the acceptable composite model to fit the spectra is a combination of a blackbody, a CEVMKL and a power law with an interstellar absorption (tbabs) together with a constant which yields the foremost χ^2_ν of 1.05 (see Fig. 2.5-bottom). A blackbody model to fit these soft excesses can be inferred that the system has an optically thick boundary layer as we expected at high accretion rate. We note that the N_H is fixed during the fitting process because yielding too low values.

As we fixed the neutral hydrogen column density to $N_H = 2.3 \times 10^{21}$, the best-fit model yields $kT_{max} = 23.3^{+6.6}_{-4.0}$ keV for the maximum plasma temperature, $\alpha = 0.8^{+0.08}_{-0.08}$ for the powerlow index of the distribution of the temperature and $K_{CEVMKL} = 1.9^{+0.1}_{-0.2} \times 10^{-4}$ for the CEVMKL normalization. In addition, solar abundances of elements aside from Oxygen and Iron were calculated to be $4.3^{+1.2}_{-0.9}$ $1.9^{+0.4}_{-0.3}$, respectively. For the POWERLAW parameters the fit yields $3.9^{+0.34}_{-0.29}$ and $1.9^{+0.4}_{-0.4} \times 10^{-4}$ for photon index and normalization, respectively. The fit also gives a blackbody temperature $kT = 26.0^{+1.0}_{-1.0}$ eV with a normalization K$_{bbody}$ =

---

[1] `http://www.swift.ac.uk/analysis/nhtot/index.php`

[2] `https://heasarc.gsfc.nasa.gov/xanadu/xspec/manual/XSmodelBbody.html`

[3] `https://heasarc.gsfc.nasa.gov/xanadu/xspec/manual/XSmodelPowerlaw.html`

Table 2.2: Spectral Parameters of the best-fit model to the SS Aur Spectra

Model	Component	Value
tbabs	$N_H(\times10^{22}cm^{-2})$	0.23 (Fixed)
constant		$0.95^{+0.02}_{-0.02}$
bbody	$kT(eV)$	$26.0^{+1.0}_{-1.0}$
	$K_{bbody}(\times10^{-3})$	$6.7^{+2.0}_{-2.0}$
	$F_{BB}(\times10^{-10}ergs^{-1}cm^{-2})$	$2.5^{+0.9}_{-0.8}$
	$L_{X,BB}(\times10^{33}ergs^{-1})$	$1.2^{+0.4}_{-0.4}$
powerlaw	$PhoIndex$	$4.0^{+0.3}_{-0.3}$
	$K_{POWERLAW}(\times10^{-4})$	$1.9^{+0.4}_{-0.4}$
	$F_{PO}(\times10^{-11}ergs^{-1}cm^{-2})$	$1.5^{+0.2}_{-0.8}$
	$L_{X,PO}(\times10^{31}ergs^{-1})$	$7.2^{+8.5}_{-3.6}$
CEVMKL	$kT_{max}(keV)$	$23.3^{+6.6}_{-4.0}$
	$K_{CEVMKL}(\times10^{-3})$	$1.9^{+0.1}_{-0.2}$
	$alpha$	$0.8^{+0.08}_{-0.08}$
	O	$4.2^{+1.2}_{-0.9}$
	Fe	$1.9^{+0.4}_{-0.3}$
	$F_{CEV}(\times10^{-12}ergs^{-1}cm^{-2})$	$4.4^{+0.6}_{-0.6}$
	$L_{X,CEV}(\times10^{31}ergs^{-1})$	$2.1^{+0.3}_{-0.3}$
χ^2_ν (dof)		1.05 (588)
F_{unabs}	$(\times10^{-10}ergs^{-1}cm^{-2})$	$2.7^{+1.1}_{-0.9}$
$L_{X,unabs}$	$(\times10^{33}ergs^{-1})$	$1.3^{+0.5}_{-0.4}$

N_H is the absorbing neutral hydrogen column density for the *tbabs* which was fixed at 0.23 $\times10^{22}cm^{-2}$ to improve the quality of the fit. kT_{max} is the maximum temperature for the CEVMKL model. K_{CEVMKL} is the normalization for the CEVMKL model, O and Fe show the variation of the Oxygen and Iron from solar abundances. *PhoIndex* is the photon index of power law and $K_{POWERLAW}$ is the normalization of powerlaw with the unit of photons keV^{-1} cm^{-2} s^{-1} at 1 keV. K_{bbody} $(\frac{L_{39}}{D_{10}^2})$, where L_{39} is the source luminosity in units of 10^{39} erg s^{-1}, D_{10} is the distance to the source in units of 10 kpc. F_{BB} is the flux of blackbody radiation calculated in the energy range of 0.1 - 10.0 keV. F_{PO} and F_{CEV} are the fluxes calculated in 0.1 - 50.0 keV using the models powerlaw and CEVMKL respectively. $L_{X,BB}$, $L_{X,PO}$ and, $L_{X,CEV}$ are the X-ray luminosities calculated using the related fluxes of each model. F_{unabs} and $L_{X,unabs}$ are the unabsorbed flux and X-ray luminosity of the source. All errors are given at 90% confidence limit for a single parameter.

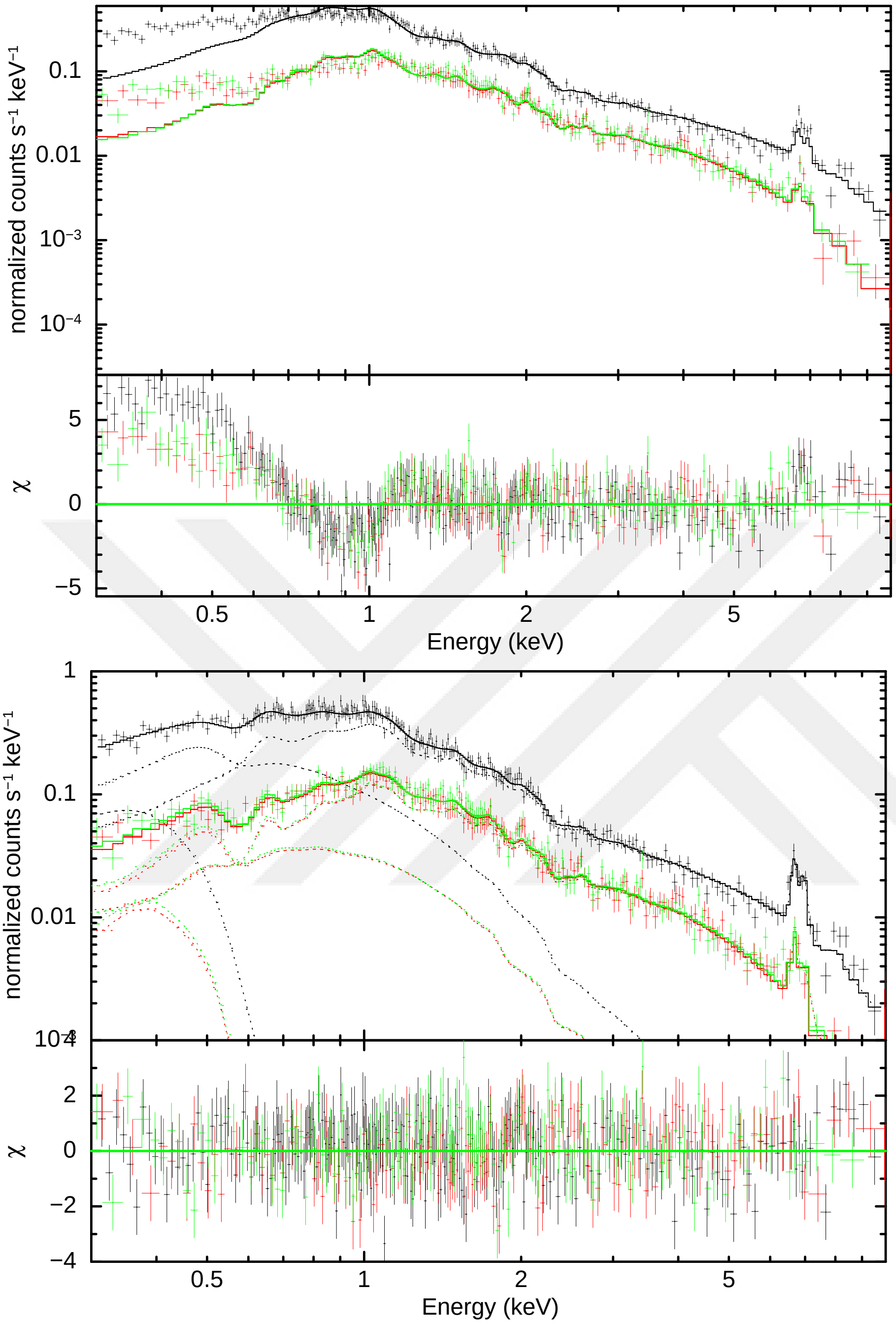

Figure 2.5: Top: The upper panel shows the combined EPIC pn (black), MOS 1 (red) and MOS 2 (green) spectra of SS Aur together with the composite model [(tbabs*constant*(CEVMKL)] fitted to the spectra and the lower panel shows the residuals in the standard deviation. Bottom: The upper panel shows the same EPIC spectra of SS Aur together with the best composite model [(tbabs*constant*(bbody+powerlaw+CEVMKL)] fitted to the spectra. The dashed lines show individual additive model components on the data plots. The lower panel shows the residuals in standard deviations.

$5.19^{+1.49}_{-1.51} \times 10^{-3}$. All the errors were obtained at the 90% confidence level.

The unabsorbed X-ray flux is $2.7^{+1.1}_{-0.9} \times 10^{-10}$ erg s^{-1} cm^{-2} in energy range of 0.1-50.0 keV translates to an X-ray luminosity of $1.3^{+0.5}_{-0.4} \times 10^{33}$ erg s^{-1} at the $\sim$ 200 pc source distance. In addition, using the equation [66]

$$L_{acc} = G\dot{M}M_{WD}/2R_{WD} \tag{2.1}$$

where L_{acc} is the accretion luminosity, $\dot{M}$ is the accretion rate onto the white dwarf surface and M_{WD} and R_{WD} are the mass and radius of the white dwarf. By taking $M_{WD} = 1.03\ M_{\odot}$ [97] and $R_{WD} = 5.6 \times 10^{8}$ which is calculated using Nauenberg [109] mass-radius relation for a 1 $M_{\odot}$ white dwarf, we obtained the mass accretion rate of SS Aur to be $1.75^{+0.7}_{-0.5} \times 10^{-10}\ M_{\odot}$ yr^{-1}.

We also tried other composite models to fit the spectra. We used two APEC (Astrophysical Plasma Emission Code; Smith et al. [110]) models to obtain the temperature distribution in the boundary layer of the source instead of CEVMKL. We have used two APEC plasma models together with a blackbody and a power law with an interstellar absorption (*tbabs*). This fit yielded $4.8^{+0.4}_{-0.7}$ and $0.95^{+0.03}_{-0.04}$ keV as the thermal plasma temperatures. In addition, It yields a χ^2_{ν} of 1.25 (dof 589) which is worse than the fits with the multi-temperature plasma model over 5σ significance level (obtained from F-test probability). The other model sets we used to fit the spectra are different combinations of APEC model with *tbabs* without considering the blackbody and power law models. We tried one APEC model together with a *tbabs* and again two APECs with a *tbabs*. The yielded χ^2_{ν} of both of the composite models were higher that 2. Then, we applied three APEC models with an interstellar absorption (*tbabs*) to the spectra. The fit yields different plasma temperatures for each APEC model as $0.8^{+0.04}_{-0.1}$, $1.9^{+0.2}_{-0.3}$ and $10.1^{+0.8}_{-0.7}$ keV which show the distribution of thermal plasma temperatures. The reduced χ^2 of the fit is 1.17 (dof 590) which again is worse than our best model fit over 5σ significance level. The N_H was fixed at 2.3×10^{21} in all the composite models.

Table 2.3: System Physical Parameters of EY Cyg

Parameter	Unit	EY Cyg
M_{wd}	$M_{\odot}$	1.10 ± 0.09
M_{2nd}	$M_{\odot}$	0.49 ± 0.09
i	deg	14^a
P	day	0.459323(3)
T_0	HJD	2449255.337(5)
d	pc	450
V_{min}		14.8
V_{max}		11

Echevarria et al. [112]; Sion et al. [116];

2.3.2 EY Cyg

EY Cygni has been detected by ROSAT observatory in the energy range of 0.4 – 2.2 keV (soft X-Rays) [111]. It is a U Gem type star with an orbital period of 11.023752 h derived from Hα emission line analysis and the ephemeris is T_0 = 2449255.337(5) [112]. The system parameters are given in Table 2.3. The visual magnitudes of the system during quiescent and outburst are $\sim$ 14.8 and $\sim$ 11, respectively. The analysis of long term AAVSO light curves revealed that the recurrence time for the system is about 2000 days [113] which is 8 times longer than the previously measured cycle by Piening [114]. Early studies of EY Cyg revealed that the it contains a WD with a mass of M_{wd} = 1.26 and a secondary with M_{sec} = 0.59 $M_{\odot}$. Later, Echevarria et al. [112] using photometric analysis derived the masses as $M_{wd} = 1.10 \pm 0.09$ $M_{\odot}$ and $M_{sec} = 0.49 \pm 0.09$ $M_{\odot}$ which confirms that the WD is massive consistent with Costero et al. [115] and Sion et al. [116]. In addition, they found that the system has an inclination angle of 14 degrees. The spectral type of the secondary in this system is not fully determined. However, in 1962 Kraft estimated that the spectral type of the secondary to be K0V [44]. Later, Smith et al. [117] in a survey of 22 objects, using spectral analysis with ISIS triple-beam spectrograph classified the secondary of EY Cyg to be in the range K5 - M0.

There is no a certainty for the distance of EY Cyg, however, we give a brief summary about different determinations of the system distance below. According to Warner [5] the distance of a system can be calculated using the relation between absolute magnitude at outburst ($M_{V,max}$) and orbital period of the source. Considering this, EY Cyg should be at a distance of 505 pc. Another estimation for the distance of EY Cyg implies that the system is placed in a range of 250 – 700 pc [113, 116]. The lower limit is calculated based on the spectral type of the secondary. The upper limit also was determined based on the X-Ray luminosity which shows that the source is not embedded in the Cygnus supper-bubble. Tovmassian et al. [113] found the system to be in 400 – 500 pc. In far-UV spectral analysis of EY Cyg during FUSE and Hubble Space Telescope (HST) observation done by Sion et al. [116], an average distance of 450 pc was adopted. Their best model fit yielded a distance of 391 pc which is in the estimated range. Their modeling also shows EY Cyg contains white dwarf with T_{eff} = 22000 K and accretion belt with T_{eff} = 36000 K.

2.3.2.1 Timing Analysis

The same procedure of timing analysis were performed for EY Cyg. The EPIC light curves were extracted with bin time of 0.1 s and plotted with a bin time of 100 s. Three EPIC light curves are shown in Fig. 2.6-top. We then combined all the background-subtracted light curves (EPIC pn, MOS1 and MOS2) as one and folded it over the orbital period of the system (11.023752 h) using 8 phase bins in order to study the orbital variations in the X-rays. We used the ephemeris of T_0 = 2449255.337(5) where the zero phase correspond to the inferior conjunction of the secondary star ([112], Fig. 2.6-bottom). The orbital modulation behaviour in EY Cyg folded light curve are sinusoidal with a minima and maxima of 0.5 and 1.0, respectively. It also shows a 2.5 phase shift in comparison with the radial-velocity curve derived from Hα variations [112]. In order to investigate the phase variation of the binary components, primary and secondary, we separate the light curves according to their energy into two light curves. In the first one, we considered the energies between 300 – 600 eV and the second one was considered in the range 800 – 8000 eV. Using two different epochs, the start time

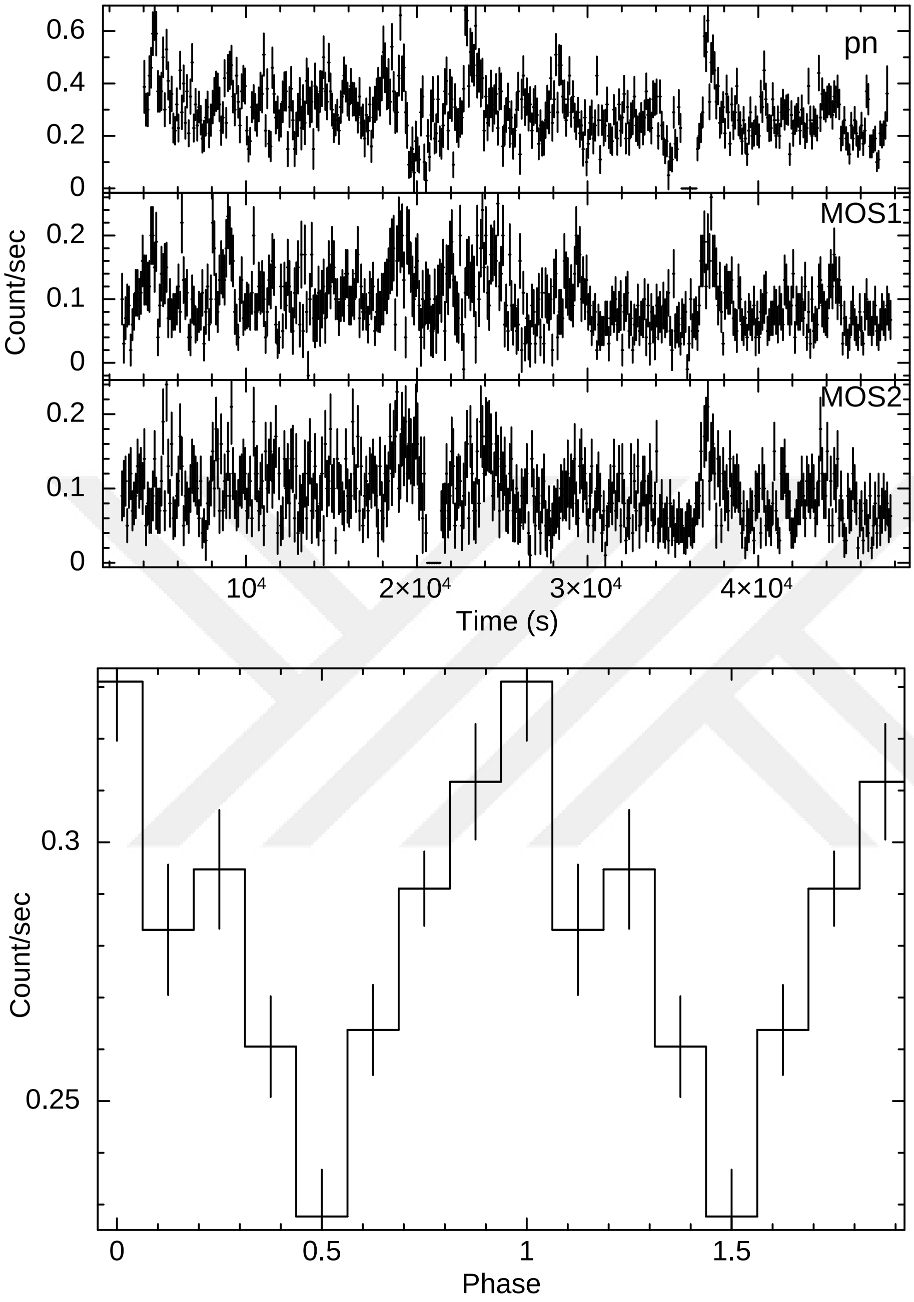

Figure 2.6: Top: The *XMM-Newton* EPIC light curves of EY Cyg plotted with the bin time size of 100 s. Bottom: The combined EPIC light curves folded of the orbital period of 11.023752 h with $T_0 = 2449255.337(5)$ [112].

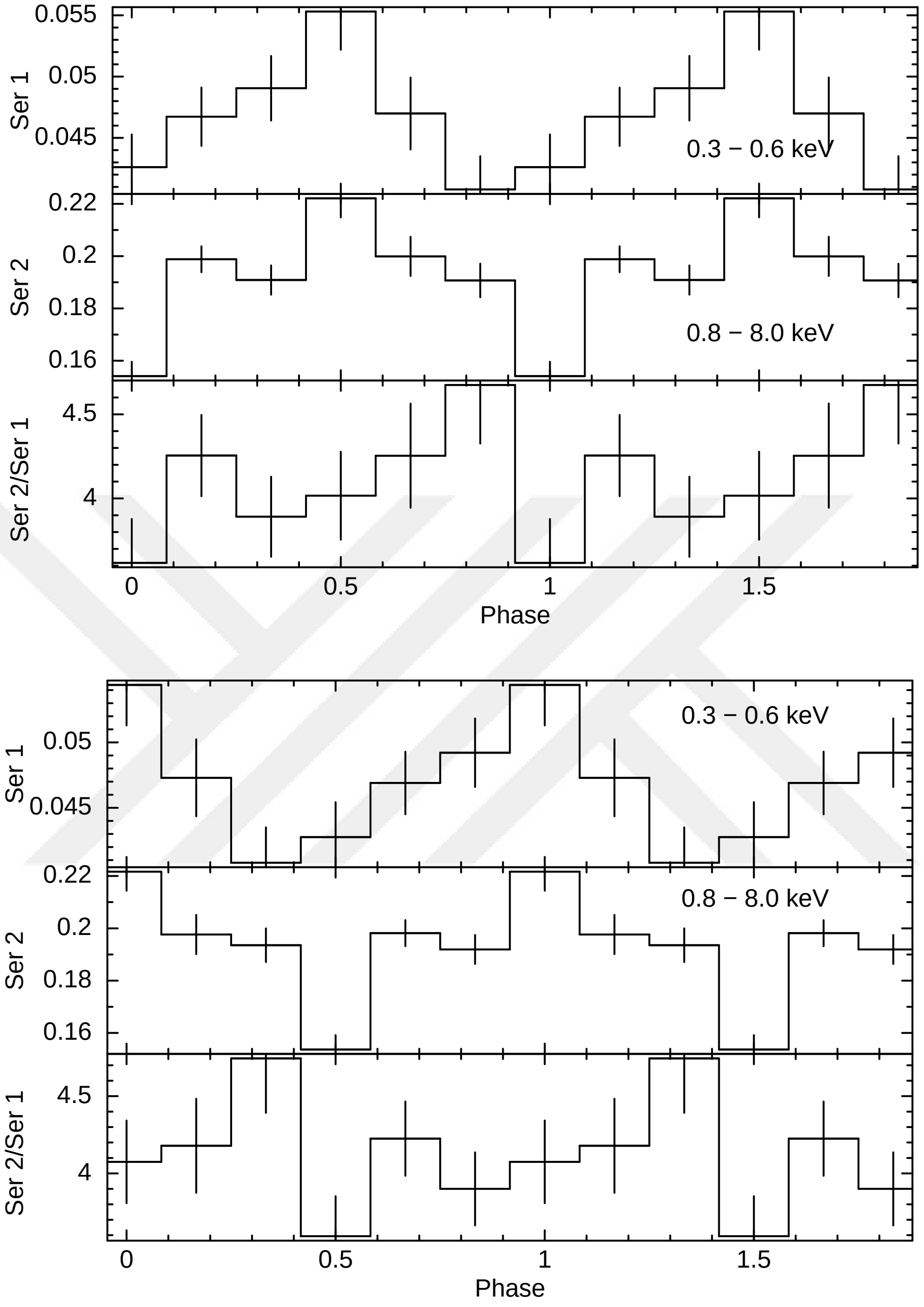

Figure 2.7: Hardness ratio of folded X-ray light curves of EY Cyg over the orbital period in two different energy bands of 0.3 – 0.6 kev and 0.8 – 8.0 keV. Top: the epoch of our observation was used to extract the folded light curves; Bottom: the ephemeris of $T_0 = 2449255.337(5)$ Echevarria et al. [112] was considered as the epoch for extracting the folded light curves.

Table 2.4: The X-Ray Luminosity of K0 Spectral Type Stars

Name/ROSAT Name	Spectral Type	Distance (pc)	L_X (erg s^{-1})
RXJ 0540.0-5343	K0V	164^{+24}_{-18}	$1.57^{+1.9}_{-1.0} \times 10^{30}$
RXJ 0548.0-6241	K0/1V	170^{+34}_{-22}	$1.6^{+2.3}_{-1.0} \times 10^{30}$
RXJ 1429.4-0049	K0V	87^{+6}_{-6}	$1.2^{+0.5}_{-0.4} \times 10^{30}$
RXJ 1433.3-0126	K0/1V	506^{+116}_{-75}	$12.3^{+19.2}_{-8.0} \times 10^{30}$

Adopted from Metanomski et al. [118]

of the observation and the epoch of the ephemeris in [112], we again folded the light curves at the orbital period of the system calculated with radial velocity variations. Then, we plotted the hardness ratio of the two folded light curves with different energy bands using LCURVE (Fig. 2.7). As clearly seen in the plots, there is a phase shift of ~ 0.2 phase in the minima. The phase-shifted minima indicates that the origins of the X-ray modulations for the soft band light curve (0.3 – 0.6 keV) and the hard band light curve (0.8 – 8.0 keV) are different.

2.3.2.2 Spectral Analysis

As discussed in section 2.3.1.2, we used the same tasks to extract the EPIC spectra. The spectra then were grouped to have 55 counts in each energy bin for pn and 30 counts for MOS1 and MOS2. The spectra have average count rates of 0.34, 0.1 and 0.1 count/s for pn, MOS1 and MOS2, respectively. The photons with the energies below than 0.3 keV and higher than 9.0 keV were ignored. The spectral fitting was simultaneously performed for all three EPIC spectra using an absorption for interstellar medium (*tbabs*) together with a single temperature plasma model (MEKAL) [106, 119] and a multi-temperature plasma emission model (CEVMKL). The spectral parameters are given in Table 2.5. The spectra of pn, MOS1 and MOS2 are shown in the Fig. 2.8 together with the best-fit model.

The CEVMKL model was used to fit the hard X-rays emitted from the boundary layer as expected in low accretion rate quiescent dwarf novae. In order to fit the soft X-ray excess of the spectra, in our first attempt, we added a blackbody component to the composite model. However, the fit yielded unacceptable blackbody temperature and normalization. This gave the idea that the origin of the soft excess may not be the boundary layer but the secondary star. Therefore, instead of the blackbody model used a MEKAL model to fit the soft X-rays originating from the secondary which is a K-type star.

Numerous observations provided by the early generation of space X-ray observatories like Einstein, ROSAT and, EXOSAT have shown that all late-type main sequence stars are powerful X-ray emitters. During a photometric and low resolution spectroscopic analysis, Metanomski et al. [118] investigated the spectral classification and X-ray luminosity of about 46 selected stars of type F, G and K observed by ROSAT in its all-sky survey. The mean X-ray luminosity they found for their samples is in the range of 10^{29} – 10^{30}. In the Table 2.4, we summarized the information of four K0-type stars they selected. According to this work and another analysis done by Gudel [120] the X-ray luminosity of K-type stars can be roughly estimated to be around 10^{30} erg s^{-1}. The best composite model we used to fit the spectra yields a MEKAL temperature of $kT_{MEKAL} = 0.1^{+0.02}_{-0.01}$ keV and $K_{MEKAL} = 2.7^{+1.3}_{-1.3} \times 10^{-5}$ which are valid for a K-type secondary. The X-ray flux emerged from the secondary in the energy range of 0.1 – 50.0 keV is $F_{sec} = 5.6^{+3.2}_{-2.9} \times 10^{-14}$ erg s^{-1} cm^{-2}) which translates to an X-ray luminosity of $L_{X,sec} = 1.4^{+0.4}_{-0.4} \times 10^{30}$ erg s^{-1}. The X-ray luminosity we obtained for the secondary is consistent with the previous measured X-ray luminosities for K0 spectral type stars. The X-ray light curve modulation in the energy range of 0.3 – 0.6 keV in comparison with the X-ray modulation in the energy range of 0.8 – 8.0 confirms that the soft X-ray emerges from a different place (secondary star) that the harder X-ray is emerged.

According to nhtot [108], the value of neutral hydrogen column density for EY Cyg is 9.48×10^{21} atoms cm^{-2}. However, considering that the optical reddening of the system is E(V-B) = 0.0 [121], the N_H should be lower than this. In our fit, N_H was calculated to be $0.04^{+0.02}_{-0.01} \times 10^{22} cm^{-2}$. Using the relation between the optical reddening and the hydrogen column density $N_H = 5 \times 10^{21}\ E(V-B)^4$, our N_H gives an optical reddening of 0.08 mag which is more or less consistent

---

[4] `https://heasarc.nasa.gov/Tools/w3nh_help.html`

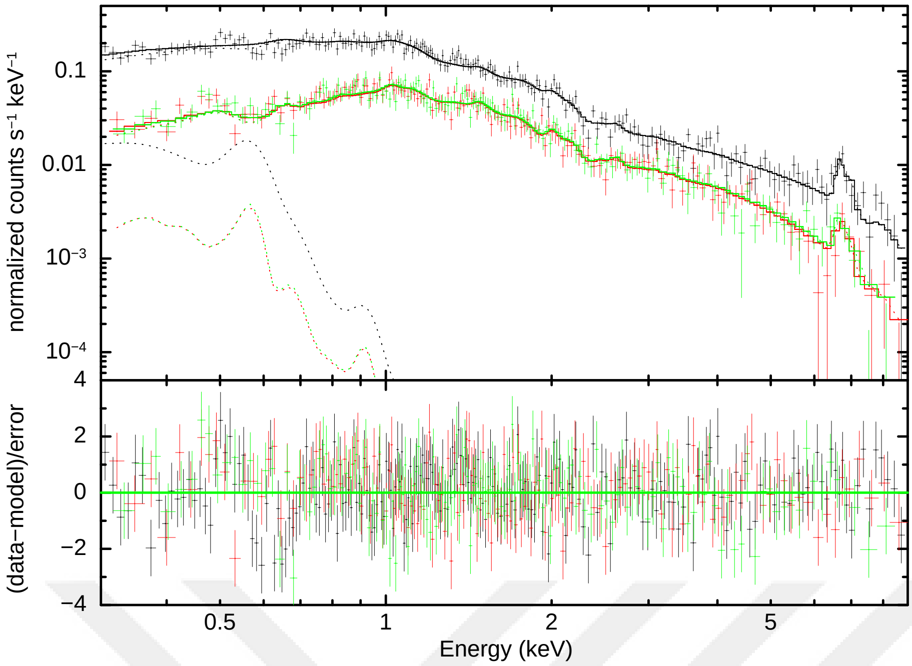

Figure 2.8: The upper panel shows the combined EPIC PN (black), MOS 1 (red) and MOS 2 (green) spectra of EY Cyg together with the composite model [(tbabs*constant*(MEKAL+CEVMKL)] fitted to the spectra and the dashed lines show individual additive model components on the data plots. The lower panel shows the residuals in standard deviations.

with the low reddening of the system. The best-fit model yields $kT_{max} = 14.9^{+3.3}_{-2.2}$ keV for the maximum plasma temperature, $\alpha = 1.2^{+0.2}_{-0.2}$ for the powerlow index of the temperature distribution and $K_{CEVMKL} = 1.6^{+0.2}_{-0.2} \times 10^{-3}$ for the CEVMKL normalization. All the errors were obtained at the 90% confidence level.

The unabsorbed X-ray flux is $1.9^{+0.1}_{-0.1} \times 10^{-12}$ erg s^{-1} cm^{-2} in energy range of 0.1-50.0 keV which translates to an X-ray luminosity of $2.1^{+0.3}_{-0.3} \times 10^{31}$ erg s^{-1} at the $\sim$ 450 pc source distance. In addition, using the equation 2.1 and by taking $M_{WD} = 1.1\ M_{\odot}$ and $R_{WD} = 6 \times 10^{8}$ [109], we obtained a mass accretion rate estimation for EY Cyg as $1.1^{+0.2}_{-0.3} \times 10^{-12}\ M_{\odot}$ yr^{-1}.

Table 2.5: Spectral Parameters of the best fit model to the EY Cyg Spectra

Model	**Component**	**Value**
tbabs	$N_H(\times 10^{22} cm^{-2})$	$0.04^{+0.02}_{-0.01}$
constant		$0.98^{+0.03}_{-0.03}$
MEKAL	$kT(KeV)$	$0.1^{+0.01}_{-0.02}$
	$K_{MEKAL}(\times 10^{-5})$	$2.7^{+1.3}_{-1.3}$
	$F_{MKL}(\times 10^{-14} ergs^{-1} cm^{-2})$	$5.6^{+3.2}_{-2.9}$
	$L_{X,MKL}(\times 10^{30} ergs^{-1})$	$1.4^{+0.4}_{-0.4}$
CEVMKL	$kT_{max}(keV)$	$14.9^{+3.3}_{-2.2}$
	$K_{CEVMKL}(\times 10^{-3})$	$1.6^{+0.2}_{-0.2}$
	$alpha$	$1.2^{+0.2}_{-0.2}$
	$F_{CEV}(\times 10^{-12} ergs^{-1} cm^{-2})$	$1.9^{+0.1}_{-0.1}$
	$L_{X,CEV}(\times 10^{31} ergs^{-1})$	$2.1^{+0.3}_{-0.3}$
χ^2_ν (dof)		1.04 (527)

N_H is the absorbing neutral hydrogen column density for the *tbabs*. kT is the plasma temperature for the *MEKAL* model. K_{MEKAL} is the normalization for the MEKAL model. kT_{max} is the maximum temperature for the CEVMKL model. K_{CEVMKL} is the normalization for the CEVMKL model. F_{MKL} is the unabsorbed X-ray flux of the secondary star calculated in the energy range of 0.1 - 50.0 keV using the MEKAL model. F_{CEV} is the unabsorbed X-ray flux emerged from the boundary layer calculated in 0.1 - 50.0 keV using the model CEVMKL. $L_{X,MKL}$ is the X-ray luminosity of the K-type secondary and $L_{X,CEV}$ is X-ray luminosity of the source. Both are calculated using the related fluxes of each model. All errors are given at 90% confidence limit for a single parameter.

CHAPTER 3

SWIFT OBSERVATIONS

3.1 Observatory and Instruments

SWIFT is a multi-wavelength observatory which was launched into a low-Earth orbit at 17:16 GMT on 20th November 2004, on a Delta II 7320-10C expendable launch vehicle [122]. It is designed to study Gamma-Ray Burst (GRB) in different energy bands suck as gamma-ray, X-ray, optical, and ultraviolet wavebands. To cover such a wide energy band, *SWIFT* has three instruments (Fig. 3.1) on board such as Burst Alert Telescope (BAT), X-Ray Telescope (XRT), Ultraviolet-Optical Telescope (UVOT; [123]). It can detect the location of a burst with the accuracy of 4 arcminutes in 10 seconds. After the burst detection is done, *SWIFT* points the narrow field of view XRT and UVOT at the source in 20 – 70 seconds for continued afterglow studies. *SWIFT* had detected more than 1000 GRBs till November 2015 with a discovering rate of approximately 100 bursts per year.

The *SWIFT* X-Ray Telescope (XRT) is a sensitive X-ray imaging spectrometer which operates in the energy range of 0.2 – 10 keV with a FOV of 23.6 arcmin square [124]. It is designed to measure fluxes, light curves and spectra of GRBs and afterglows. The XRT uses an X-ray CCD detector with a Wolter 1 mirror set of 3.5 m focal length that is similar to EPIC MOS on *XMM-Newton*. Depending on the flux of the afterglow, the XRT operates in three different modes: Imaging (IM), Photon Counting (PC), and Windowed Timing (WT). The XRT automatically selects a proper mode depending on the brightness of the source. This procedure allows the XRT to observe sources in a range of 7 orders of magnitude in flux.

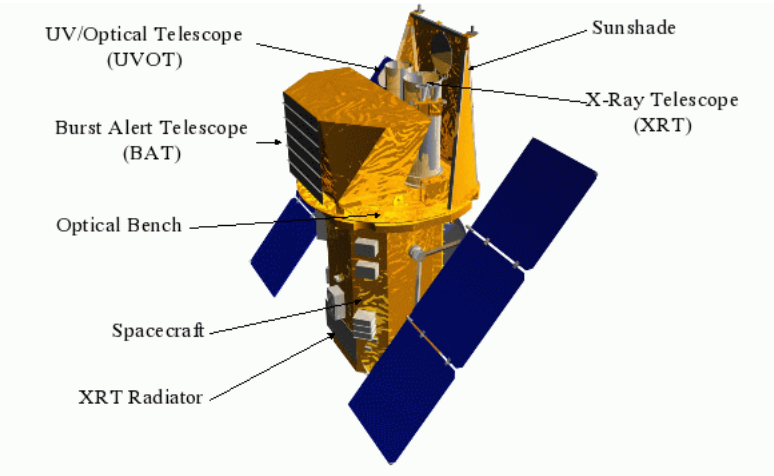

Figure 3.1: Schematics for the SWIFT observatory and its on-board instruments. Taken from http://www.swift.ac.uk/about/instruments.php.

Imaging mode data is used only to localize the position of a new GRB. The photon counting mode uses full imaging and spectroscopic resolution at very low fluxes. It has a time resolution of 2.51 seconds. The windowed timing mode obtains high resolution timing with a time resolution of 1.7×10^{-3} seconds. There was another mode called Photo-Diode mode (PD) which was disabled since the end of May 2005. The Burst Alert Telescope is a coded aperture imaging telescope which is designed to monitor a large fraction of the space to detect the occurrences of GRBs [125]. It is a highly sensitive instrument with a 1.4 steradians field of view (approximately comparable with a single human eye) which can cover an energy range of 15 – 150 keV. In this chapter, we report on the analysis of the XRT and BAT data of the TW Pic obtained in the photon counting (PC) mode.

3.2 Data and Observation

The archival *SWIFT* data of TW Pic were reduced and analysed using XSELECT V2.4b and HEASoft 6.17[1]. To produce the cleaned event files (level 2) from level 1 products, we used the **xrtpipeline** tool with the standard criteria. We also check the positions of the sources using **xrtcentroid**. TW Pic

---

[1] `http://heasarc.nasa.gov/lheasoft/`

was observed by *SWIFT* observatory on 13 November 2007 (00037120001), 25 December 2007 (00037120002), 31 December 2007 (OBSID: 00037120003), 19 December 2015 (00034215001) and again 19 December 2015 (00034215002). The details of the observations were given in the Table 3.1. These observations provide a total 18.5 ks of exposure time. In this chapter, just the XRT (PC mode) data of these observations was considered. The X-ray spectra and light curves were extracted from all the five data sets using circular regions with a radius of 20 arcsec. The background spectra and light curves, likewise, were extracted from a source-free region on the same chip. To extract the light curves in the energy range of 0.3-10 keV, the event files were filtered using PHA_CUTOFF 30 1000.

In the spectral analysis, in order to have good statistics and also by considering the dates of the observations, we separated them into three groups. The first observation itself took as the first group. Though, it obtained in the same year with the second and third observations however, there is a 42-day of time lag between them and also shows different characteristics in its spectrum. The second group was made up by merging the second and third observations (obtained in December 2007). The Third group as well as the second one was made by merging the forth and fifth observations (obtained in December 2015). Three spectra were extracted from these groups.

The calibration file of version 20010101v014 (released on 20 Dec 2013 on the SWIFT data base) and the standard grade filtering (0–12 for PC) were used for the analysis. In order to calculate the ancillary response files for each group, we first merged the exposure maps of the related observations using the **xrtexpomap** task in XIMAGE and then, we performed the task **xrtmkarf**. The temporal and spectral analysis of TW Pic using *SWIFT* observations are explained in the following sections.

Table 3.1: *SWIFT* Observation Details of TW Pic

No	Obs ID	Date (UT) (yyyy-mm-dd)	Time (UT) (hh:mm:ss)	Exp. Time (s)	XRT Mode
1	00037120001	2007-11-13	01:25:15	6000	PC
2	00037120002	2007-12-25	12:07:01	2800	PC
3	00037120003	2007-12-31	15:40:01	7000	PC
4	00034215001	2015-12-19	17:21:58	400	PC/WT
5	00034215002	2015-12-19	17:26:58	2250	PC/WT

3.3 Analysis and Results

3.3.1 TW Pic

TW Pic (*SWIFT J0535.1-5801*) is a cataclysmic variable suggested as an Intermediate Polar (section 1.1.3) based on its extended flux ratio and its strong He II emission line [33]. It has an average V magnitude of $\sim$ 14.9 [126]. For the first time, Tuohy et al. [126] suggested that the TW Pic might be a DQ Her system by reporting the optical identification of the hard X-ray source 23 H 0534–581. In their next study of TW Pic, Buckley and Tuohy [127] obtained a mass of 0.6 $M_\odot$ for the secondary by using the empirical mass-period relation of Patterson [128]. Using the secondary mass function $f(M_2) = P_{orb}K_1^3/2\pi G = (M_2 sini)^3/(M_1 + M_2)^2$, they estimated the system inclination between $i =$ 18° – 26° for a range of white dwarf mass 0.6 – 1.4 $M_\odot$. With regard to the range of mass which we assumed for the white dwarf (0.7 – 1.0 $M_\odot$) the inclination is $i =$ 19° – 22°. They also calculated an orbital period of 6.5 h for the system. However, the optical photometric study of TW Pic by Patterson and Moulden [129] revealed that the orbital period of the system is 6.06 ± 0.03 h. According to the same paper, the ephemeris of the system is HJD = 2448207.785(14) (minimum light). TW Pic is located at a distance of $\sim$ 617 pc (`http://vizier.u-strasbg.fr/viz-bin/VizieR-4?-c=TW%20Pic&-c.rs=10&-kw.Wavelength=optical&-ucd=*pos.*`;[130]) in the coordinates of RA = 05 34 50.60 and DEC = -58 01 40.7. The system parameters are given in Ta-

Table 3.2: System Physical Parameters of TW Pic

Parameter	Unit	TW Pic
M_{wd}	$M_\odot$	0.7–1.0[a]
M_{2nd}	$M_\odot$	0.6 [b]
i	*deg*	19–22 [b]
P	*day*	0.2525[c]
T_0	*HJD*	2448207.785[c]
d	*pc*	617[d]
V		14.9[e]

[a] As explained in the section 3.3.1, the WD mass is unknown and we assumed a lower and an upper limit for it; [b]Buckley and Tuohy [127]; [c]Patterson and Moulden [129]; [d]Ozdonmez et al. [130]; [e]tuohy1986identification

ble 3.2. In the following sections, we report the analysis of the XRT data of TW Pic obtained in the photon counting (PC) mode for a total exposure time of 18.5 ks.

3.3.1.1 Temporal Analysis

In order to correct the event times, the solar system barycentric correction was applied to all the five event files. Using XSELECT we first combined the event files to obtain three data groups as we explained in the section 3.2. The standard light curve extraction procedures were used to extract the XRT light curves between 0.3 - 10.0 keV with a 2.51 s time resolution. The individual light curves of the first and third observations are shown in the Fig. 3.2. To search for the variations of the X-ray light curve, we folded them over the orbital period of the system using 5 phase bins. The results are displayed in the Fig. 3.3.

For the orbital period, we used the 6.06 ± 0.03 h. Since the accumulated phase error as a result of the error in the orbital period was large, we could not lock the phases of the different observations to the optical ephemerides Patterson and Moulden [129] used in their study. Therefore, the date of the first detected photon was used as the epoch for each folded light curve. Although, the orbital modulation behaviour in both folded light curves are similar (sinusoidal), however, they show phase shifts in minima and maxima. A preliminary analysis of the SWIFT data of TW Pic was presented in our poster paper Balman et al. [131] along with XMM-Newton and RXTE analysis of the data. The lack of long exposure time in each observation made it difficult to study the variations comprehensively and prevented us to do power spectral analysis.

3.3.1.2 Spectral Analysis

For the spectral analysis we use the 70-month *SWIFT*/BAT spectrum of TW Pic simultaneously with the *SWIFT*/XRT spectra to study the source in a wider energy range. Using all the archival XRT observations separated into three groups, we extracted the XRT spectra using the standard extraction procedures as explained in the *SWIFT*/XRT analysis threads webpage[2]. The spectra then were grouped to have 60 counts in each energy bin for all three groups. Photons with the energies below than 0.3 keV and higher than 6.0 keV were ignored. The BAT 70-month spectrum is obtained in the period of December 2004 to October 2010. The BAT spectrum and its related response matrix were downloaded from the *SWIFT* webpage[3]. The BAT 70-month survey has operated in full BAT energy band of 14–195 keV. In the BAT 70-month survey, the data are extracted in eight different energy bands and then combined to a total band map. Then blind sources are roughly localized and after that the counterparts to the sources identified by searching high resolution archival X-ray data provided by *XMM-Newton*, *Chandra* and *SWIFT*-XRT [132]. The spectra have count rates of 0.37, 0.29, 0.31 and 3.3×10^{-5} count/s for group 1, group 2, group 3 and BAT, respectively. The spectral fitting was simultaneously performed for all three XRT spectra and the BAT spectrum using an absorption model *tbabs* for the interstellar medium and a partial covering neutral absorber model (*pcfabs*;

---

[2] `http://www.swift.ac.uk/analysis/xrt/`

[3] `https://swift.gsfc.nasa.gov/results/bs70mon/SWIFT_J0535.1-5801`

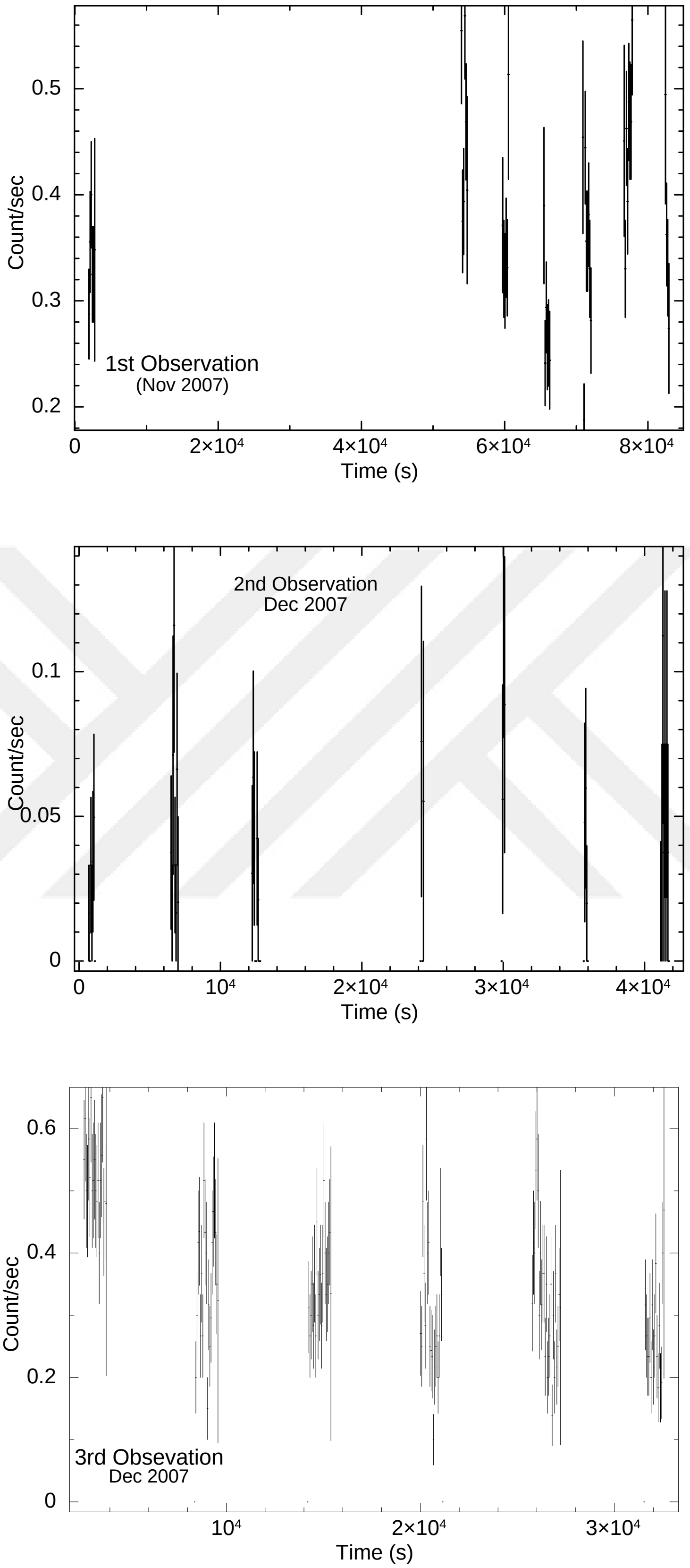

Figure 3.2: (*Top:* The *SWIFT*/XRT light curves of TW Pic extracted from the first observation (top),second observation (middle) and third observation (bottom) with a bin time of 70 s.

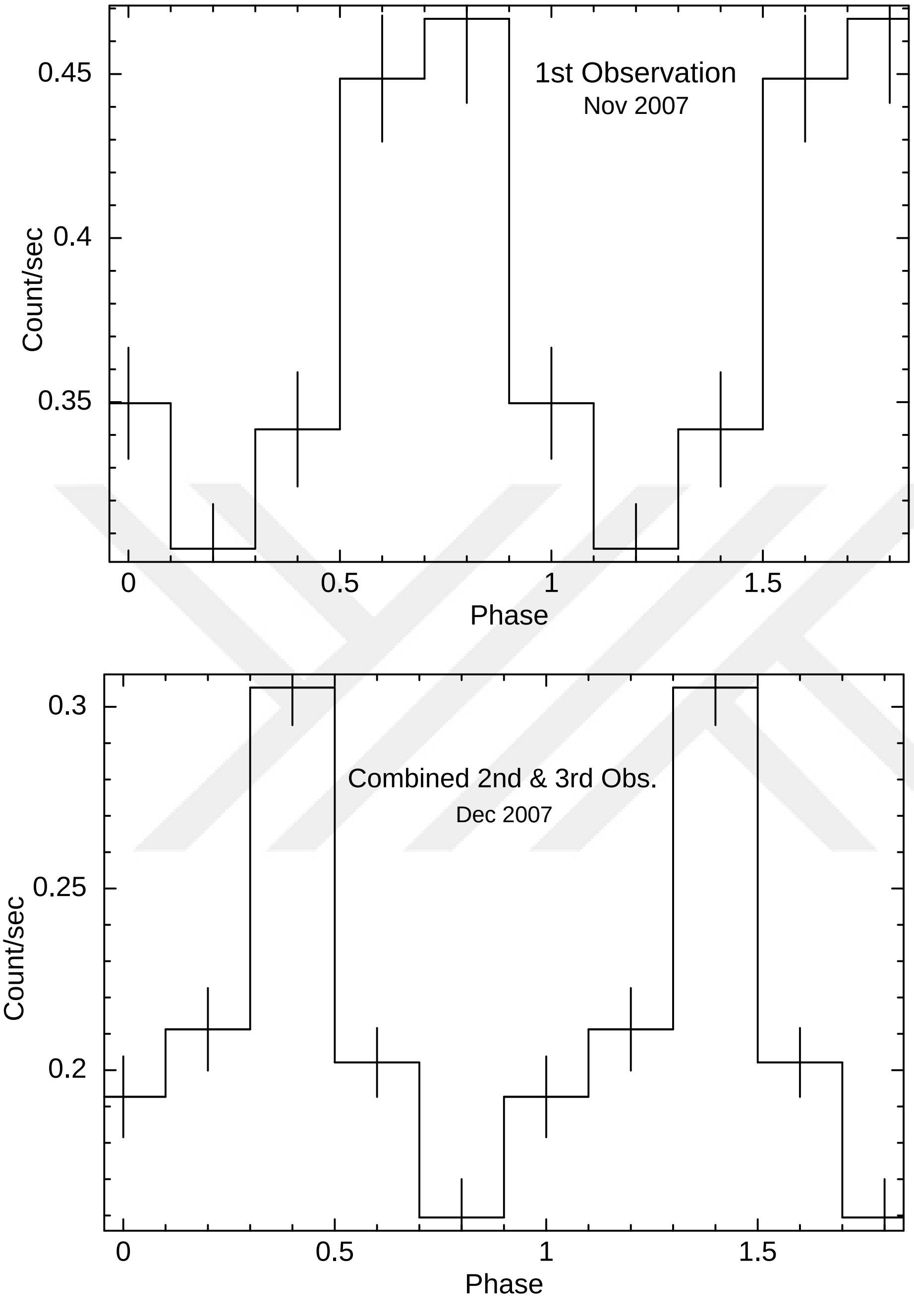

Figure 3.3: (*Top: SWIFT*/XRT light curve of the first observation of TW Pic folded over the orbital period of 6.06 h using the observation's epoch. *Bottom: SWIFT*/XRT light curve of the Second group of observations of TW Pic folded over the orbital period of 6.06 h using the observations' epoch)

$M(E) = fexp[\eta_H \sigma - (E)] + (1 - f)$, where $\sigma(E)$ is the photoelectric cross-section, η_H is the equivalent hydrogen column in units of 10^{22} atoms cm^{-2} and f is dimensionless covering fraction $(0 < f \leq 1))^4$ for the intrinsic absorption together with a multi-temperature plasma emission model CEVMKL. In order to normalize the uncertainty between XRT and BAT instruments, a constant factor was added to the fit. The spectral parameters are given in Table 3.3. The $SWIFT$-XRT spectra of group 1 to 3 and the BAT spectrum are shown in the Fig.3.4 together with the best-fit model.

We fixed the neutral hydrogen column density to $N_H = 5\times\ 10^{20}$ cm^{-2} according to nhtot (Willingale et al. [108]). The free parameters in the *pcfabs* model are the absorption column (N_H^{pcfabs}) and the covering fraction ($CvrFract$) which we keep them varying for all the data groups during the fitting process. N_H^{pcfabs} for XRT spectra of groups 1 to 3 are $4.0^{+3.0}_{-2.0}$, $2.0^{+1.2}_{-0.7}$ and, $1.5^{+1.0}_{-0.6}$, respectively. In addition, the covering fractions are $0.5^{+0.07}_{-0.08}$, $0.4^{+0.1}_{-0.1}$ and $0.6^{+0.1}_{-0.1}$ for data groups 1 to 3, respectively. For the BAT spectrum, we found N_H^{pcfabs} and $CvrFract$ zero as expected in higher energy bands. The best-fit model yields $kT_{max} = 26.5^{+6.0}_{-4.5}$ keV for the maximum plasma temperature, $\alpha = 1.1^{+0.3}_{-0.3}$ for the powerlow index of the distribution of the temperature and $K_{CEVMKL} = 3.4^{+0.9}_{-0.7} \times 10^{-2}$ for the CEVMKL normalization. The composite model gave a χ^2_ν of 1.12 (dof 81).

For TW Pic, we calculated an unabsorbed X-ray flux of $5.2^{+0.7}_{-0.3}\ \times 10^{-11}$ erg s^{-1} cm^{-2} in the energy range of 0.1 – 50 keV which translates to an X-ray luminosity of $2.4^{+0.3}_{-0.2}\ \times 10^{33} ergs^{-1}$. Since the mass of white dwarf in TW Pic is unknown, we used a lower limit of $M_{WD} = 0.7\ M_\odot$ ($R_{WD} = 8.0 \times 10^8$) and an upper limit of $M_{WD} = 1.0\ M_\odot$ ($R_{WD} = 5.8 \times 10^8$) to calculate the accretion rate. At a distance of $\sim$ 617 pc, we obtained the mass accretion rate of TW Pic to be $6.5^{+0.9}_{-0.5} \times 10^{-10}\ M_\odot$ yr^{-1} and $3.3^{+0.4}_{-0.3} \times 10^{-10}\ M_\odot$ yr^{-1} for the assumed lower and upper limit of WD mass, respectively. Our result are consistent with previous works on IPs [133, 134].

As we discussed before, to have good statistics we separated the observations into three groups. However, since the BAT observation does not cover the 2015 observations and also to investigate the spectral characteristics of every sin-

---

[4] `https://heasarc.gsfc.nasa.gov/xanadu/xspec/manual/node240.html`

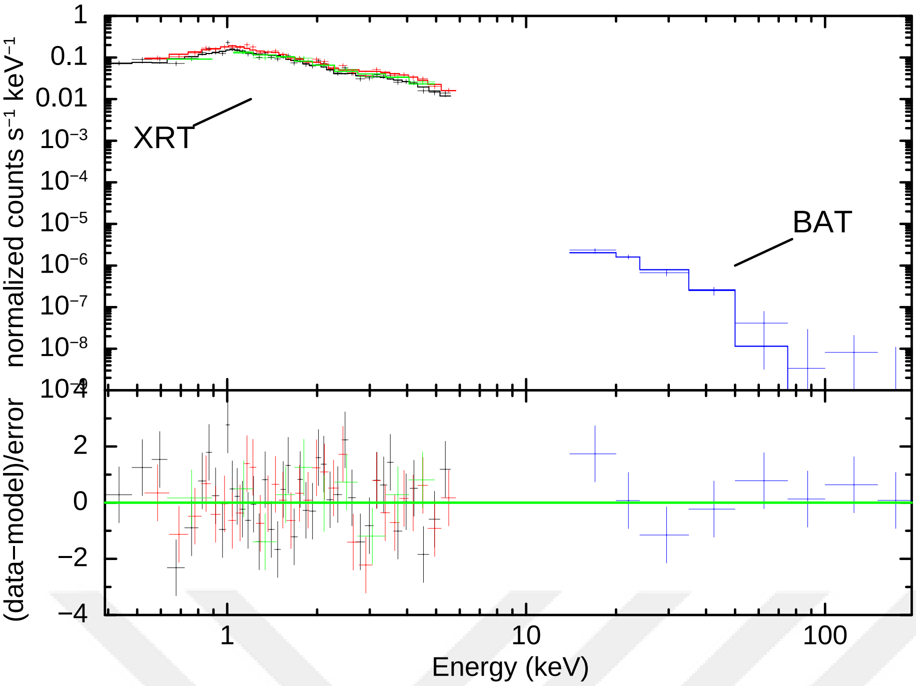

Figure 3.4: The upper panel shows the *SWIFT*/XRT and *SWIFT*/BAT spectra of TW Pic together with the composite model [(tbabs*pcfabs*constant*(CEVMKL)] fitted to the spectra and the lower panel shows the residuals in the standard deviations.

gle observation, we applied the spectral fitting to the individual XRT spectra separately. The results show that the unabsorbed X-ray flux, luminosity and averaged accretion rate vary in the range of (0.1 – 1.0) × 10^{-10} erg s^{-1} cm^{-2}, (0.55 – 4.5) × 10^{33} erg s^{-1} and (1.1 – 9.1) × 10^{-10} $M_\odot$ yr^{-1}, respectively.

In addition, we found $F_X = 2.0 \times 10^{-10}$ erg s^{-1} cm^{-2}, $L_X = 9.1 \times 10^{33}$ erg s^{-1} and $\dot{M} = 1.9 \times 10^{-9}$ $M_\odot$ yr^{-1} for the BAT spectrum. The BAT survey spectrum has a spatial resolution of 21 arcmin per pixel centered best to about 3 arcmin. This indicates that our BAT spectrum may have contamination from other sources. In our previous work, we also combined all the XRT observations and fit the combined spectrum with the same composite model (Please see the table of spectral parameters in [131].

We have recently studied TW Pic [131] using two *XMM-Newton* and one *RXTE* observations of TW Pic along with the *SWIFT* observation. The *XMM-Newton* and *RXTE* data were obtained on March–April 2008 and May 1999, respectively. The authors used two different composite model to fit the XMM-Newton spectra. The first, is a model composition of *tbabs* and *pcfabs* together with a CEVMKL and two *Gaussians* in 6.4 and 6.7 keV. In the second one, they added a blackbody component to both XMM-Newton observations and found a blackbody temperature of $\sim$ 20 eV only in one of the observations. We did not detect any Iron line in the energies of 6.4 and 6.7 keV through the *SWIFT* observations. In this work, we also added a blackbody component to our best fit model, but, it did not make any improvement to the *SWIFT* fit.

In our previous poster paper, Balman et al. [131], we found an unabsorbed X-ray luminosity $1 - 3 \times 10^{33}$ erg s^{-1} and an accretion rate $3 - 5 \times 10^{-10}$ $M_{\odot}$ yr^{-1} for the *XMM-newton* and *RXTE* data of TW Pic which are consistent with those we calculated using *SWIFT* observations. It indicates that TW Pic has a steady state and does not change dramatically through the years 1999 to 2015. Our best-fit model yields a high partial covering absorber of $\sim$ 2.5 (averaged) $\times 10^{22}$ cm^{-2} for the XRT spectra which is in the range of the ones we expect from IPs [135, 136]. This also is consistent with the partial covering absorbers we found for the *XMM-Newton* and *RXTE* spectral analysis [131].

Table 3.3: Spectral Parameters of the best-fit model to the TW Pic $SWIFT$/XRT-BAT Spectra

Model		**Component**	**Value**
tbabs		$N_H(\times10^{22}cm^{-2})$	0.05 (Fixed)
constant			$0.72^{+0.09}_{-0.09}$
pcfabs	XRT-G1	$N_H(\times10^{22}cm^{-2})$	$3.8^{+3.0}_{-1.6}$
		CvrFract	$0.5^{+0.07}_{-0.08}$
	XRT-G2	$N_H(\times10^{22}cm^{-2})$	$2.0^{+1.2}_{-0.7}$
		CvrFract	$0.4^{+0.1}_{-0.1}$
	XRT-G3	$N_H(\times10^{22}cm^{-2})$	$1.4^{+1.0}_{-0.6}$
		CvrFract	$0.6^{+0.1}_{-0.1}$
	BAT	$N_H(\times10^{22}cm^{-2})$	0.0
		CvrFract	0.0
CEVMKL		$kT_{max}(keV)$	$26.5^{+5.8}_{-4.5}$
		$K_{CEVMKL}(\times10^{-2})$	$3.3^{+0.9}_{-0.7}$
		$alpha$	$1.07^{+0.3}_{-0.3}$
χ^2_ν (dof)			1.12 (91)
F$_{unabs}$		$(\times10^{-11}ergs^{-1}cm^{-2})$	$5.2^{+0.7}_{-0.3}$
L$_{X,unabs}$		$(\times10^{33}ergs^{-1})$	$2.4^{+0.3}_{-0.2}$

The XRT-Group 1 is the first observation itself obtained in November 2007. The XRT-Group 2 is the combined second and third observations obtained in Dec 2007. XRT-Group 3 is the combined forth and fifth observations obtained in December 2015. N_H is the absorbing neutral hydrogen column density for the *tbabs* which was fixed at 0.23 $\times10^{22}cm^{-2}$ to improve the quality of the fit. kT_{max} is the maximum temperature for the CEVMKL model. K$_{CEVMKL}$ is the normalization for the CEVMKL model. *CvrFrac* is the covering fraction. of the absorber. F$_{unabs}$ and L$_{X,unabs}$ are the unabsorbed flux and X-ray luminosity of the source calculated in 0.1 - 50.0 keV. All errors are given at 90% confidence level (2σ) for a single parameter.

CHAPTER 4

SUMMARY AND CONCLUSIONS

X-ray analysis of cataclysmic variables provides us significant information about the accretion procedure, accretion disks and X-ray emission in binary systems. CVs are important samples to study the mass transfer in binary star systems. In this work, we reviewed the X-ray temporal and spectral characteristics of three cataclysmic variables SS Aur, EY Cyg and TW Pic during their quiescence state. SS Aur and EY Cyg are non-magnetic systems and TW Pic is a magnetic CV candidate suggested as an Intermediate Polar (IP). We applied different composite models to fit the spectra of these systems. The main results of this work is summarized in the Table 4.1. In this chapter, we present a brief summary of the results we obtained from our studies and analysis.

- **SS Aur.** We fitted the spectra of SS Aur using a composite model of *tbabs×constant(bbody+powerlaw+CEVMKL)* and obtained an X-ray luminosity of 1.3 × 10^{33} erg s^{-1} and an accretion rate of 1.75 × 10^{-10} $M_{\odot}$ yr^{-1} for SS Aur. The fit yielded a maximum plasma temperature of 23.3 keV and a blackbody temperature of 26 eV. We also found two elements of Oxygen and Iron over abundances as 4.3 and 1.9, respectively. Existence a balckbody component in the spectra of a quiescent dwarf nova which is expected to has an optically thin boundary layer, suggests that the boundary layer may not have the standard characteristics. There are phase shifts between the optical UV and X-ray folded mean light curves over the orbital period. It may because of hotspot at the accretion impact zone as seen in CVs. No periodicity or coherent QPO were detected in SS Aur PSDs because of high levels of red noise.

- **EY Cyg.** The X-ray spectra of EY Cyg were fitted by a composite model of *tbabs×pcfabs×constant(MEKAL+CEVMKL)* which yielded an X-ray luminosity of 2.1×10^{31} erg s^{-1} and an accretion rate of 1.1×10^{-12} $M_\odot$ yr^{-1} as expected from a low state quiescent dwarf nova of EY Cyg. According to the fit, the system has a maximum plasma temperature of 14.9 keV. The folded light curve of EY Cyg shows a minima and maxima at the phases 0.5 and 1.0, respectively. There is a 2.5 phase shift in both minima and maxima in comparison with the radial-velocity curve derived from Hα variations by Echevarria et al. [112]. We also fitted the soft X-ray excess emerged from the secondary star using a MEKAL model. We calculated the luminosity and temperature of the secondary star as $L_{X,sec} = 1.4 \times 10^{30}$ erg s^{-1}) and $kT = 0.1$ keV. As we discussed in the chapter section 2.3.2.2, these results are valid for a K-type secondary. In addition, the X-ray modulation in the energy range of 0.3 – 0.6 keV shows phase-shifted minima with regard to those in the range of 0.8 – 8.0 keV. These analysis, in the X-ray domains, confirms that the secondary in EY Cyg is a K-type star. Based on the X-ray luminosity we calculated for the secondary, it probably is a K0 star, which has been estimated by [44].

- **TW Pic.** The XRT spectra and BAT spectrum were simultaneously fitted by a composite model of *tbabs×pcfabs×constant(CEVMKL)*. The X-ray luminosity and the accretion rate for TW Pic were calculated to be 2.3×10^{33} erg s^{-1} and 4.75×10^{-10} $M_\odot$ yr^{-1}, respectively. These results are consistent with the values Brunschweiger et al. [133] and Landi et al. [134] found for numerous selected IP systems. In addition, yielding a high partial covering absorber (similar to those IPs show in general) for the XRT spectra, our model suggests that the TW Pic could be an IP. We did not detect any blackbody component for the source. However, since Balman et al. [131] detected a balckbody component using *XMM-newton* observation of TW Pic, we suggest that the lack of blackbody emission in the *SWIFT* observations may due to the accretion curtains obstruction of the polar caps [40] or the *SWIFT* poor sensitivity in the soft band. The source shows variations in N_H in the range (3.8 – 1.4) $\times 10^{22}$ cm^{-2} and unabsorbed X-ray flux and luminosity in the range of (0.1 – 1.0) $\times 10^{-10}$ erg s^{-1} cm^{-2} and (0.55 – 4.5) $\times 10^{33}$ erg s^{-1} over the span of years 2007 – 2015.

Table 4.1: The results of the spectral analysis of three selected sources SS Aur, EY Cyg and TW Pic

Source	**Composite Model**	χ^2_ν	$\mathbf{kT}_{max}$ (keV)	$\mathbf{F}_X$ (erg s^{-1} cm^{-2})	$\mathbf{L}_X$ (erg s^{-1})	$\dot{\mathbf{M}}$ ($M_\odot$ yr^{-1})
SS Aur	tbabs×constant(bbody+powerlaw+CEVMKL)	1.05	23.3	2.7×10^{-10}	1.3×10^{-10}	1.75×10^{-10}
EY Cyg	tbabs×constant(MEKAL+CEVMKL)	1.04	14.9	1.9×10^{-12}	2.1×10^{31}	1.1×10^{-12}
TW Pic	tbabs×pcfabs×constant(CEVMKL)	1.12	26.5	5.2×10^{-11}	2.4×10^{33}	4.9×10^{-10}

kT_{max} is the maximum temperature for the *CEVMKL* model. F_X and L_X are the unabsorbed flux and X-ray luminosity of the sources calculated in 0.1 - 50.0 keV. $\dot{M}$ is the accretion rate of the systems

REFERENCES

[1] L. Eyer and N. Mowlavi. Variable stars across the observational hr diagram. In *Journal of Physics: Conference Series*, volume 118, page 012010. IOP Publishing, 2008.

[2] J. R. Hind. On a new variable star. *Monthly Notices of the Royal Astronomical Society*, 16:56–56, 1856.

[3] R. A. Downes, R. F. Webbink, Ronald F., M. M. Shara, H. Ritter, U. Kolb, and H. W. Duerbeck. A catalog and atlas of cataclysmic variables: the final edition. *arXiv preprint astro-ph/0602278*, 2006.

[4] K. Mukai. X-ray emissions from accreting white dwarfs: A review. *Publications of the Astronomical Society of the Pacific*, 129(976):062001, 2017.

[5] B. Warner. *Cataclysmic variable stars*, volume 28. Cambridge University Press, 2003.

[6] S. Balman. The x-ray properties of cataclysmic variables. *Mem. Societa Astronomica Italiana*, 83:585, 2012.

[7] D. Branch, M. Livio, L. R. Yungelson, F. R. Boffi, and E. Baron. In search of the progenitors of type ia supernovae. *Publications of the Astronomical Society of the Pacific*, 107(717):1019, 1995.

[8] B. Warner. Cataclysmic variable stars (cambridge astrophysics series, cambridge, new york, 1995.

[9] C. Hellier. *Cataclysmic Variable Stars-how and why they vary.* Springer Science and Business Media, 2001.

[10] M. M. Shara. Recent progress in understanding the eruptions of classical novae. *Publications of the Astronomical Society of the Pacific*, 101(635): 5, 1989.

[11] M. Kato. Recurrent novae, classical novae, symbiotic novae, and population ii novae. *arXiv preprint astro-ph/0110312*, 2001.

[12] D. M. Townsley and L. Bildsten. Classical novae as a probe of the cataclysmic variable population. *The Astrophysical Journal*, 628(1):395, 2005.

[13] S. Balman. Pre-outburst chandra observations of the recurrent nova t pyxidis. *Astronomy and Astrophysics*, 572:A114, 2014.

[14] S. Starrfield, W. M. Sparks, and J. W. Truran. Recurrent novae as a consequence of the accretion of solar material onto a 1.38 solar mass white dwarf. *The Astrophysical Journal*, 291:136–146, 1985.

[15] G. C. Anupama and J. Mikolajewska. Recurrent novae at quiescence: systems with giant secondaries. 1999.

[16] G. C. Anupama. The recurrent nova class of objects. In *RS Ophiuchi (2006) and the Recurrent Nova Phenomenon*, volume 401, page 31, 2008.

[17] S. Balman. Inner Disk Structure of Dwarf Novae in the Light of X-Ray Observations. *Acta Polytechnica CTU Proceedings*, 2:116–122, January 2015.

[18] F. Meyer and E. Meyer-Hofmeister. A model for the standstill of the z camelopardalis variables. *Astronomy and Astrophysics*, 121:29–34, 1983.

[19] V. Buat-Ménard, J. M. Hameury, and J. P. Lasota. Z cam stars: A particular response to a general phenomenon. *Astronomy and Astrophysics*, 369(3):925–931, 2001.

[20] M. Simonsen, T. Bohlsen, F. J. Hambsch, and R. Stubbings. St chamaeleontis and bp coronae australis: Two southern dwarf novae confirmed as z cam stars. *arXiv preprint arXiv:1402.0210*, 2014.

[21] J. Patterson, J. Kemp, D. A. Harvey, R. E. Fried, R. Rea, B. Monard, L. M. Cook, D. R. Skillman, T. Vanmunster, G. Bolt, et al. Superhumps in cataclysmic binaries. xxv. q crit, ξ (q), and mass-radius. *Publications of the Astronomical Society of the Pacific*, 117(837):1204, 2005.

[22] R. Whitehurst. Numerical simulations of accretion discs–i. superhumps: a tidal phenomenon of accretion discs. *Monthly Notices of the Royal Astronomical Society*, 232(1):35–51, 1988.

[23] S. Balman, P. Godon, and E. M. Sion. Swift x-ray telescope observations of the nova-like cataclysmic variables mv lyr, bz cam, and v592 cas. *The Astrophysical Journal*, 794(1):84, 2014.

[24] P. Rodríguez-Gil, B. T. Gaensicke, and et al. Sw sextantis stars: the dominant population of cataclysmic variables with orbital periods between 3 and 4 h. *Monthly Notices of the Royal Astronomical Society*, 377(4): 1747–1762, 2007.

[25] E. M. Sion. On the nature of the ux ursa majoris-type nova-like variables-cpd-48 deg 1577. *The Astrophysical Journal*, 292:601–605, 1985.

[26] C. S. Froning, K. S. Long, and C. Knigge. Accretion and outflow in interacting binary systems: Far ultraviolet spectroscopic explorer observations of the nova-like cataclysmic variable ux ursae majoris. *The Astrophysical Journal*, 584(1):433, 2003.

[27] J. Patterson, H. Uthas, J. Kemp, and et al. Bk lyncis: the oldest old nova and a bellwether for cataclysmic variable evolution. *Monthly Notices of the Royal Astronomical Society*, 434(3):1902–1919, 2013.

[28] A. R. King and J. P. Lasota. Accretion on to highly magnetized white dwarfs. *Monthly Notices of the Royal Astronomical Society*, 188(3):653–668, 1979.

[29] H. Ritter and U. Kolb. Catalogue of cataclysmic binaries, low–mass x-ray binaries and related objects. *Astronomy and Astrophysics*, 404(1):301–303, 2003.

[30] M. Cropper. The polars. *Space Science Reviews*, 54(3-4):195–295, 1990.

[31] G. Ramsay, K. O. Mason, M. Cropper, M. G. Watson, and K. L. Clayton. Rosat observations of an uma and mr ser: the status of the soft x-ray excess in am her stars. *Monthly Notices of the Royal Astronomical Society*, 270 (3):692–702, 1994.

[32] J. Lasota. Magnetic cataclysmic variables: a summary. In *International Astronomical Union Colloquium*, volume 190, pages 365–368. Cambridge University Press, 2004.

[33] J. Patterson. The dq herculis stars. *Publications of the Astronomical Society of the Pacific*, 106(697):209, 1994.

[34] E. J. Barlow, C. Knigge, A. J. Bird, A. J. Dean, D. J. Clark, A. B. Hill, M. Molina, and V. Sguera. 20–100 kev properties of cataclysmic variables detected in the integral/ibis survey. *Monthly Notices of the Royal Astronomical Society*, 372(1):224–232, 2006.

[35] R. Landi, L. Bassani, A. J. Dean, A. J. Bird, M. Fiocchi, A. Bazzano, J. A. Nousek, and J. P. Osborne. Integral/ibis and swift/xrt observations of hard cataclysmic variables. *Monthly Notices of the Royal Astronomical Society*, 392(2):630–640, 2008.

[36] J. Brunschweiger, J. Greiner, M. Ajello, and J. Osborne. Intermediate polars in the swift/bat survey: spectra and white dwarf masses. *Astronomy and Astrophysics*, 496(1):121–127, 2009.

[37] D. De Martino, G. Matt, K. Mukai, and et al. 1rxs j173021. 5-055933: a cataclysmic variable with a fast-spinning magnetic white dwarf. *Astronomy and Astrophysics*, 481(1):149–159, 2008.

[38] A. Staude, A. D. Schwope, R. Schwarz, J. Vogel, M. Krumpe, and A. N. Gomez-Moran. The changing accretion states of the intermediate polar mu camelopardalis. *Astronomy and Astrophysics*, 486(3):899–909, 2008.

[39] G. Anzolin, D. De Martino, J. M. Bonnet-Bidaud, M. Mouchet, B. T. Gaensicke, G. Matt, and K. Mukai. Two new intermediate polars with a soft x-ray component. *Astronomy and Astrophysics*, 489(3):1243–1254, 2008.

[40] P. A. Evans and C. Hellier. Why do some intermediate polars show soft x-ray emission? a survey of xmm-newton spectra. *The Astrophysical Journal*, 663(2):1277, 2007.

[41] A. J. Norton, G. A. Wynn, and R. V. Somerscales. The spin periods and magnetic moments of white dwarfs in magnetic cataclysmic variables. *The Astrophysical Journal*, 614(1):349, 2004.

[42] A. J. Norton, O. W. Butters, T. L. Parker, and G. A. Wynn. The accretion flows and evolution of magnetic cataclysmic variables. *The Astrophysical Journal*, 672(1):524, 2008.

[43] K. Mukai, A. Kinkhabwala, J. R. Peterson, S. M. Kahn, and F. Paerels. Two types of x-ray spectra in cataclysmic variables. *The Astrophysical Journal Letters*, 586(1):L77, 2003.

[44] R. P. Kraft. Binary stars among cataclysmic variables. i. u geminorum stars (dwarf novae). *Astrophysical Journal*, 135:408, March 1962.

[45] B. Warner. Observations of rapid blue variables–xiv: Zc hamaeleontis. *Monthly Notices of the Royal Astronomical Society*, 168(1):235–247, 1974.

[46] S. H. Lubow and F. H. Shu. Gas dynamics of semidetached binaries. *The Astrophysical Journal*, 198:383–405, 1975.

[47] S. H. Lubow and F. H. Shu. Gas dynamics of semidetached binaries. ii-the vertical structure of the stream. *The Astrophysical Journal*, 207:L53–L55, 1976.

[48] F. Verbunt and C. Zwaan. Magnetic braking in low-mass x-ray binaries. *Astronomy and Astrophysics*, 100:L7–L9, 1981.

[49] A. Einstein. *Relativity: The special and the general theory.* Princeton University Press, 2015.

[50] B. P. Abbott, R. Abbott, and et al. Observation of gravitational waves from a binary black hole merger. *Physical review letters*, 116(6):061102, 2016.

[51] S. Rappaport, F. Verbunt, and P. C. Joss. A new technique for calculations of binary stellar evolution, with application to magnetic braking. *The Astrophysical Journal*, 275:713–731, 1983.

[52] J. Frank, A. King, and D. Raine. Accretion power in astrophysics. *Cambridge Astrophysics Series*, 21, 1992.

[53] J. Frank, A. King, and D. Raine. *Accretion power in astrophysics*. Cambridge university press, 2002.

[54] N. I. Shakura and R. A. Sunyaev. Black holes in binary systems. observational appearance. *Astronomy and Astrophysics*, 24:337–355, 1973.

[55] D. Lynden-Bell and J. E. Pringle. The evolution of viscous discs and the origin of the nebular variables. *Monthly Notices of the Royal Astronomical Society*, 168(3):603–637, 1974.

[56] S. Starrfield, C. Iliadis, and W. R. Hix. The thermonuclear runaway and the classical nova outburst. *Publications of the Astronomical Society of the Pacific*, 128(963):051001, 2016.

[57] R. D. Gehrz, J. W. Truran, R. E. Williams, and S. Starrfield. Nucleosynthesis in classical novae and its contribution to the interstellar medium. *Publications of the Astronomical Society of the Pacific*, 110(743):3, 1998.

[58] M. F. Bode and A. Evans. *Classical novae*, volume 43. Cambridge University Press, 2008.

[59] Y. Osaki. An accretion model for the outbursts of u geminorum stars. *Publications of the Astronomical Society of Japan*, 26:429–436, 1974.

[60] R. C. Smith. Cataclysmic variables. *Contemporary Physics*, 47(6):363–386, 2006.

[61] B. Warner. Observations of rapid blue variables—vii ex h ydrae. *Monthly Notices of the Royal Astronomical Society*, 158(4):425–429, 1972.

[62] S. Rappaport, W. Cash, R. Doxsey, J. McClintock, and G. Moore. Possible detection of very soft x-rays from ss cygni. *The Astrophysical Journal*, 187: L5, 1974.

[63] J. Heise, R. Mewe, and et al. Detection of both soft and hard x-ray emission from ss cygni with ans. *Astronomy and Astrophysics*, 63:L1–L3, 1978.

[64] S. Balman, P. Godon, E. M. Sion, J. U. Ness, E. Schlegel, P. E. Barrett, and P. Szkody. Xmm-newton observations of the dwarf nova ru peg in quiescence: Probe of the boundary layer. *The Astrophysical Journal*, 741 (2):84, 2011.

[65] J. Patterson and J. C. Raymond. X-ray emission from cataclysmic variables with accretion disks. i-hard x-rays. ii-euv/soft x-ray radiation. *The Astrophysical Journal*, 292:535–558, 1985.

[66] D. Lynden-Bell and J. E. Pringle. The evolution of viscous discs and the origin of the nebular variables. *Monthly Notices of the Royal Astronomical Society*, 168(3):603–637, 1974.

[67] F. Verbunt, W. H. Bunk, H. Ritter, and E. Pfeffermann. Cataclysmic variables in the rosat pspc all sky survey. *Astronomy and Astrophysics*, 327:602–613, 1997.

[68] D. S. Baskill, P. J. Wheatley, and J. P. Osborne. The complete set of asca x-ray observations of non-magnetic cataclysmic variables. *Monthly Notices of the Royal Astronomical Society*, 357(2):626–644, 2005.

[69] P. Godon, O. Regev, and G. Shaviv. One-dimensional time-dependent numerical modelling of accretion disc boundary layers. *Monthly Notices of the Royal Astronomical Society*, 275(4):1093–1101, 1995.

[70] E. Kuulkers, A. Norton, A. Schwope, and B. Warner. X-rays from cataclysmic variables. *in Compact stellar X-ray sources, ed. W. Lewin & M. van der Klis, Cambridge Astrophysics Series*, 39:421–460, 2006.

[71] T. Belloni, F. Verbunt, , K. Beuermann, and et al. Rosat observation of the boundary layer between the white dwarf and the accretion disk of vw hydri. *Astronomy and Astrophysics*, 246:L44–L46, 1991.

[72] A. van Teeseling, K. Beuermann, and F. Verbunt. The x-ray source in non-magnetic cataclysmic variables. *Astronomy and Astrophysics*, 315: 467–474, 1996.

[73] G. J. Ferland, G. H.and Pepper, S. H. Langer, J. MacDonald, J. W. Truran, and G. Shaviv. The mystery of the missing boundary layer. *The Astrophysical Journal*, 262:L53–L58, 1982.

[74] A. van Teeseling and F. Verbunt. Rosat x-ray observations of ten cataclysmic variables. *Astronomy and Astrophysics*, 292:519–533, 1994.

[75] F. Meyer and E. Meyer-Hofmeister. Accretion disk evaporation by a coronal siphon flow. *Astronomy and Astrophysics*, 288:175–182, 1994.

[76] T. J. Ponman, T. Belloni, S. R. Duck, F. Verbunt, M. G. Watson, P. J. Wheatley, and E. Pfeffermann. The euv/x-ray spectrum of ss cygni in outburst. *Monthly Notices of the Royal Astronomical Society*, 276(2):495–504, 1995.

[77] M. Livio and J. E. Pringle. Dwarf nova outbursts–the ultraviolet delay and the effect of a weakly magnetized white dwarf. *Monthly Notices of the Royal Astronomical Society*, 259(1):23P–26P, 1992.

[78] J. Patterson and J. C. Raymond. X-ray emission from cataclysmic variables with accretion disks. i-hard x-rays. ii-euv/soft x-ray radiation. *The Astrophysical Journal*, 292:535–558, 1985.

[79] R. Narayan and R. Popham. Hard x-rays from accretion disk boundary layers. *Nature*, 362(6423):820–822, 1993.

[80] R. Popham. A boundary layer origin for dwarf nova oscillations. *Monthly Notices of the Royal Astronomical Society*, 308(4):979–983, 1999.

[81] K. Mukai, J. H. Wood, T. Naylor, E. M. Schlegel, and J. H. Swank. The x-ray eclipse of the dwarf nova ht cassiopeiae: Results from asca and rosat hri observations. *The Astrophysical Journal*, 475(2):812, 1997.

[82] K. Mukai and K. Shiokawa. The exosat medium energy (me) sample of dwarf novae. *The Astrophysical Journal*, 418:863, 1993.

[83] R. J. Gould. Thermal bremsstrahlung from high-temperature plasmas. *The Astrophysical Journal*, 238:1026–1033, 1980.

[84] D. Pandel, F. A. Córdova, K. O. Mason, and W. C. Priedhorsky. X-ray observations of the boundary layer in dwarf novae at low accretion rates. *The Astrophysical Journal*, 626(1):396, 2005.

[85] S. Okada, R. Nakamura, and M. Ishida. Chandra hetg line spectroscopy of the nonmagnetic cataclysmic variable ss cygni. *The Astrophysical Journal*, 680(1):695, 2008.

[86] T. Güver, C. Uluyazı, M. T. Özkan, and E. Göğüş. X-ray spectral variations of u gem from quiescence to outburst. *Monthly Notices of the Royal Astronomical Society*, 372(1):450–456, 2006.

[87] C. Done and J. P. Osborne. The x-ray spectrum of the dwarf nova ss cyg in quiescence and outburst. *Monthly Notices of the Royal Astronomical Society*, 288(3):649–664, 1997.

[88] K. Mukai, J. H. Wood, T. Naylor, E. M. Schlegel, and J. H. Swank. The x-ray eclipse of the dwarf nova ht cassiopeiae: Results from asca and rosat hri observations. *The Astrophysical Journal*, 475(2):812, 1997.

[89] F. Jansen, D. Lumb, B. Altieri, and et al. Xmm-newton observatory-i. the spacecraft and operations. *Astronomy and Astrophysics*, 365(1):L1–L6, 2001.

[90] M. J. L. Turner, A. Abbey, M. Arnaud, and et al. The european photon imaging camera on xmm-newton: the mos cameras. *Astronomy and Astrophysics*, 365(1):L27–L35, 2001.

[91] L. Strüder, U. Briel, K. Dennerl, and et al. The european photon imaging camera on xmm-newton: the pn-ccd camera. *Astronomy and Astrophysics*, 365(1):L18–L26, 2001.

[92] K. O. Mason, A. Breeveld, R. Much, and et al. The xmm-newton optical/uv monitor telescope. *Astronomy and Astrophysics*, 365(1):L36–L44, 2001.

[93] J. W. Den Herder, A. C. Brinkman, S. M. Kahn, and et al. The reflection grating spectrometer on board xmm-newton. *Astronomy and Astrophysics*, 365(1):L7–L17, 2001.

[94] D. H. Lumb, N. Schartel, and F. A. Jansen. X-ray multi-mirror mission (xmm-newton) observatory. *Optical Engineering*, 51(1):011009–1, 2012.

[95] H. Ritter and U. Kolb. Catalogue of cataclysmic binaries, low–mass x–ray binaries and related objects. *Astronomy and Astrophysics Supplement Series*, 129(1):83–85, 1998.

[96] A. W. Shafter and R. P. Harkness. Spectroscopic orbits for the dwarf novae x leonis and ss aurigae. *The Astronomical Journal*, 92:658–663, 1986.

[97] J. Lake and E. M. Sion. The accretion disk and white dwarf in the u geminorum type dwarf novae uz serpentis and ss aurigae during quiescence. *The Astronomical Journal*, 122(3):1632, 2001.

[98] T. E. Harrison, B. J. McNamara, P. Szkody, and et al. Hubble space telescope fine guidance sensor astrometric parallaxesfor three dwarf novae: Ss aurigae, ss cygni, and u geminorum. *The Astrophysical Journal Letters*, 515(2):L93, 1999.

[99] A. W. Shafter. *On the masses of white dwarfs in cataclysmic binaries.* PhD thesis, California Univ., Los Angeles., 1983.

[100] E. M. Sion, F. Cheng, P. Godon, J. A. Urban, and P. Szkody. Far-ultraviolet fuse observations of the dwarf novae ss aurigae and ru pegasi in quiescence. *The Astronomical Journal*, 128(4):1834, 2004.

[101] T. E. Harrison, J. J. Johnson, B. E. McArthur, and et al. An astrometric calibration of the mv-porb relationship for cataclysmic variables based on hubble space telescope fine guidance sensor parallaxes. *The Astronomical Journal*, 127(1):460, 2004.

[102] K. Byckling, K. Mukai, J. R. Thorstensen, and J. P. Osborne. Deriving an x-ray luminosity function of dwarf novae based on parallax measurements. *Monthly Notices of the Royal Astronomical Society*, 408(4): 2298–2311, 2010.

[103] D. A. Leahy, W. Darbro, and et al. *Astrophys. J.*, 266:160–170, 1983.

[104] P. Hakala and G. Ramsay. Xmm-newton observations of oy car iii: Om light curve modelling, x-ray timing and spectral studies. *Astronomy and Astrophysics*, 416(3):1047–1055, 2004.

[105] K. A. Arnaud. Xspec: The first ten years. In *Astronomical Data Analysis Software and Systems V*, volume 101, page 17, 1996.

[106] R. Mewe, E. Gronenschild, and G. H. J. Van Den Oord. Calculated x-radiation from optically thin plasmas. v. *Astronomy and Astrophysics Supplement Series*, 62:197–254, 1985.

[107] J. Wilms, A. Allen, and R. McCray. On the absorption of x-rays in the interstellar medium. *The Astrophysical Journal*, 542(2):914, 2000.

[108] R. Willingale, R. L. C. Starling, A. P. Beardmore, N. R. Tanvir, and P. T. O'Brien. Calibration of x-ray absorption in our galaxy. *Monthly Notices of the Royal Astronomical Society*, 431(1):394–404, 2013.

[109] M. Nauenberg. Analytic approximations to the mass-radius relation and energy of zero-temperature stars. *The Astrophysical Journal*, 175:417, 1972.

[110] R. K. Smith, N. S. Brickhouse, D. A. Liedahl, and J. C. Raymond. Collisional plasma models with apec/aped: emission-line diagnostics of hydrogen-like and helium-like ions. *The Astrophysical Journal Letters*, 556(2):L91, 2001.

[111] M. Orio and H. Ogelman. Ey cygni. *International Astronomical Union Circular*, 5680, 1992.

[112] J. Echevarria, R. Michel, R. Costero, and S. Zharikov. Determination of the basic parameters of the dwarf nova ey cygni. *Astronomy and Astrophysics*, 462(3):1069–1080, 2007.

[113] G. Tovmassian, M. Orio, S. Zharikov, J. Echevarria, R. Costero, and R. Michel. Did ey cyg go through a nova explosion? In *AIP Conference Proceedings*, volume 637, pages 72–76. AIP, 2002.

[114] A. T. Piening. The u geminorum star, ey cygni, and a probable eclipsing star, v839 cygni. *Journal of the American Association of Variable Star Observers (JAAVSO)*, 6:60–61, 1978.

[115] R. Costero, J. Echevarria, and L. Pineda. Ey cygni: A test case for low inclination cataclysmic binaries. In *Bulletin of the American Astronomical Society*, volume 30, page 1156, 1998.

[116] E. M. Sion, L. Winter, J. A Urban, G. H. Tovmassian, S. Zharikov, B. T. Gänsicke, and M. Orio. Composite accretion disk and white dwarf photosphere analyses of the fuse and hubble space telescope observations of ey cygni. *The Astronomical Journal*, 128(4):1795, 2004.

[117] R. C. Smith, M. J. Sarna, M. S. Catalan, and D. H. P. Jones. The 8190- sodium doublet in cataclysmic variables—iv. a survey of 22 objects. *Monthly Notices of the Royal Astronomical Society*, 287(2):271–286, 1997.

[118] A. D. F. Metanomski, L. Pasquini, J. Krautter, G. Cutispoto, and T. A. Fleming. F, g and k stars in the rosat all-sky survey-i. photometry. *Astronomy and Astrophysics Supplement Series*, 131(2):197–208, 1998.

[119] D. A Liedahl, A. L. Osterheld, and W. H. Goldstein. New calculations of fe l-shell x-ray spectra in high-temperature plasmas. *The Astrophysical Journal*, 438:L115–L118, 1995.

[120] M. Gudel. Radio and x-ray emission from main-sequence k stars. *Astronomy and Astrophysics*, 264:L31–L34, 1992.

[121] P. Godon, E. M. Sion, P. E. Barrett, I. Hubeny, A. P. Linnell, and P. Szkody. A far ultraviolet archival study of cataclysmic variables. i. fuse and hst stis spectra of the exposed white dwarf in dwarf nova systems. *The Astrophysical Journal*, 679(2):1447, 2008.

[122] N. Gehrels, G. Chincarini, P. Giommi, and et al. The swift gamma-ray burst mission. *The Astrophysical Journal*, 611(2):1005, 2004.

[123] P. W. A. Roming, T. E. Kennedy, K. O. Mason, and et al. The swift ultraviolet/optical telescope. *Space Science Reviews*, 120(3-4):95–142, 2005.

[124] D. N. Burrows, J. Hill, J. A. Nousek, and et al. The swift x-ray telescope. *Space Science Reviews*, 120(3):165–195, 2005.

[125] S. D. Barthelmy, L. M. Barbier, J. R. Cummings, and et al. The burst alert telescope (bat) on the swift midex mission. *Space Science Reviews*, 120(3):143–164, 2005.

[126] I. R. Tuohy, D. A. H. Buckley, R. A. Remillard, H. V. Bradt, and D. A. Schwartz. Identification of two southern x-ray emitting cataclysmic variables. *The Astrophysical Journal*, 311:275–298, 1986.

[127] D. A. H. Buckley and I. R. Tuohy. H0534-581: A new intermediate polar? *The Astrophysical Journal*, 349:296–312, 1990.

[128] J. Patterson. The evolution of cataclysmic and low-mass x-ray binaries. *The Astrophysical Journal Supplement Series*, 54:443–493, 1984.

[129] J. Patterson and M. Moulden. Rapid oscillations in cataclysmic variables. x. tw pictoris (= h0534-581). *Publications of the Astronomical Society of the Pacific*, 105(689):779, 1993.

[130] A. Ozdonmez, T. Ak, and S. Bilir. Vizier online data catalog: Galactic cataclysmic variables distances (ozdonmez+, 2015). *VizieR Online Data Catalog (other)*, 220, 2015.

[131] S. Balman, N. Talebpour-Sheshvan, and A. Nabizadeh. Xmm-newton observations of tw pic in comparison with the archival swift and rxte data. In *XMM-Newton: The Next Decade*, page 73, 2016.

[132] W. H. Baumgartner, J. Tueller, C. B. Markwardt, and et al. The 70 month swift-bat all-sky hard x-ray survey. *The Astrophysical Journal Supplement Series*, 207(2):19, 2013.

[133] J. Brunschweiger, J. Greiner, M. Ajello, and J. Osborne. Intermediate polars in the swift/bat survey: spectra and white dwarf masses. *Astronomy and Astrophysics*, 496(1):121–127, 2009.

[134] R. Landi, L. Bassani, A. J. Dean, and et al. Integral/ibis and swift/xrt

observations of hard cataclysmic variables. *Monthly Notices of the Royal Astronomical Society*, 392(2):630–640, 2008.

[135] S. Balman and B. Okcu. On the different absorption components in the x-ray spectra of the intermediate polar systems. In *The X-ray Universe 2014*, 2014.

[136] D. De Martino, G. Matt, K. Mukai, and et al. The x-ray emission of the intermediate polar v 709 cas. *Astronomy and Astrophysics*, 377(2): 499–511, 2001.